EXPLORING ΛCDM EXTENSIONS WITH SPT-3G AND PLANCK DATA: 4σ EVIDENCE FOR NON-ZERO NEUTRINO MASSES AND IMPLICATIONS OF EXTENDED DARK ENERGY MODELS FOR COSMOLOGICAL TENSIONS

A. Chudaykin [a,b*], **D. Gorbunov** [b,c**], **N. Nedelko** [b***]

[a] *Université de Genève, Département de Physique Théorique,*
CH-1211, Genève 4, Switzerland

[b] *Institute for Nuclear Research of the Russian Academy of Sciences,*
117312, Moscow, Russia

[c] *Moscow Institute of Physics and Technology,*
141700, Dolgoprudny, Moscow region, Russia

We present cosmological constraints in the ΛCDM model and a set of its extensions from a dataset based on the polarization and gravitational lensing measurements from the South Pole Telescope and the large-scale ($\ell < 1000$) part of the Planck CMB temperature measurements. In all cosmological scenarios, this CMB data combination brings the clustering measurements into agreement with the low-redshift probes of large-scale structure, resolving the S_8 tension. Combining this CMB set with a full-shape treatment of the BOSS large-scale structure observations, additional BAO measurements, information from weak lensing and photometric galaxy clustering surveys, and the Pantheon supernova catalog, we find a $\sim 4\sigma$ preference for non-zero neutrino mass, $\sum m_\nu = 0.221 \pm 0.055$ eV. We also explore dynamical dark energy in the context of the Hubble tension with two phenomenological late-time approaches introducing a phantom crossing in the dark energy equation of state. For the combination of all data considered, both models predict $H_0 \simeq 68\,\mathrm{km\cdot s^{-1}\cdot Mpc^{-1}}$, in $\sim 3\sigma$ tension with the SH0ES constraint, if the supernova absolute magnitude M_B is calibrated by CMB and LSS data as a free parameter. While it is possible to achieve H_0 values consistent with SH0ES by fixing M_B to the Cepheid-derived value, that is shown to not be a valid approach as it introduces an implicit 4.5σ tension between CMB and the local Universe.

1. INTRODUCTION

Modern cosmology has made significant progress over the last decade. The most outstanding results have come from the cosmic microwave background (CMB), which remains the most precise cosmological probe to date. The Planck measurements of CMB anisotropies have provided a remarkable confirmation of the standard Λ Cold Dark Matter (ΛCDM) cosmological model, whose parameters have been determined with unprecedented accuracy. However, the increase in experimental sensitivity has led to several statistically significant tensions between the early-time CMB measurements and the low-redshift cosmological probes.

The most significant of these tensions is the discrepancy between the values of the Hubble constant (H_0) directly measured in the late Universe and those inferred from the CMB assuming the ΛCDM cosmology [1]. The local distance ladder approach utilizing photometry of 75 Milky Way Cepheids and Gaia EDR3 parallaxes yields $H_0 = 73.2 \pm 1.3\,\mathrm{km\cdot s^{-1}\cdot Mpc^{-1}}$ [2], in 4.2σ discrepancy with the Planck CMB-derived estimate under ΛCDM, $H_0 = 67.36 \pm 0.54\,\mathrm{km\cdot s^{-1}\cdot Mpc^{-1}}$ [3]. The next

* E-mail: anton.chudaykin@unige.ch
** E-mail: gorby@ms2.inr.ac.ru
*** E-mail: nikita.nedelko1999@gmail.com

SH0ES constraint, $H_0 = 73.04 \pm 1.04\,\mathrm{km \cdot s^{-1} \cdot Mpc^{-1}}$, [4] increases the tension with the CMB estimate to 5σ. This discrepancy is commonly referred to as the Hubble tension, or even the Hubble crisis. Other direct low-redshift probes have produced H_0 values consistent with SH0ES, although with considerably larger uncertainties [1]. Type Ia supernovae calibrated by the Tip of the Red Giant Branch yield a somewhat lower value, $H_0 = 69.6 \pm 1.9\,\mathrm{km \cdot s^{-1} \cdot Mpc^{-1}}$ [5]. Time-delay measurements in strongly lensed quasar systems produce $H_0 = 73.3^{+1.7}_{-1.8}\,\mathrm{km \cdot s^{-1} \cdot Mpc^{-1}}$ [6], independent of the cosmic distance ladder. After relaxing assumptions about the mass density profile of the lensing galaxies, the TDCOSMO collaboration obtains $H_0 = 74.5^{+5.6}_{-6.1}\,\mathrm{km \cdot s^{-1} \cdot Mpc^{-1}}$, and $H_0 = 67.4^{+4.1}_{-3.2}\,\mathrm{km \cdot s^{-1} \cdot Mpc^{-1}}$ by combining the time-delay lenses with non-time-delay lenses from the SLACS sample [7].

In addition to the long-standing H_0 disagreement, the low-redshift measurements predict a systematically lower clustering amplitude compared to that obtained by Planck from CMB [8]. This tension has been supported by results from the Dark Energy Survey (DES), $S_8 = 0.776 \pm 0.017$ [9]; the Kilo-Degree Survey (KiDS), $S_8 = 0.759^{+0.024}_{-0.021}$ [10]; and the Hyper Suprime-Cam (HSC) Year 3 $S_8 = 0.776^{+0.032}_{-0.033}$ [11], where the $S_8 = \sigma_8\sqrt{\Omega_m/0.3}$ parameter modulates the amplitude of the weak lensing measurements. When combined, the DES-Y3 and KiDS-1000 measurements are in tension with the Planck baseline result $S_8 = 0.832 \pm 0.013$ [3] at the 3.3σ level. Analyses of the full-shape power spectra and bispectrum data [12] along with traditional measurements of redshift-space distortions [13] also yield consistently low values of S_8. While the H_0 and S_8 tensions can hint at cracks in the standard cosmological paradigm and the necessity for new physics, these discrepancies can also be in part the result of systematic errors in the experiments.

Notably, there are a few particular features in the Planck data that lead to moderate tensions in parameter consistency tests. The most significant of these is an oscillatory residual of the temperature (TT) power spectrum in the range $1000 \lesssim \ell \lesssim 2000$ that mimics extra smoothing of acoustic CMB peaks generated by gravitational lensing [14] [1]. The amount of lensing determined from the smoothing of the acoustic peaks in the CMB spectra is 2.8σ too high when compared

---

[1] Although the oscillatory pattern looks similar to gravitational lensing at high multipoles, an implausibly large change in the foreground model can give a difference in the predicted spectra with a similar oscillatory component, see the related discussion in [14].

with the ΛCDM expectation based on the «unlensed» temperature and polarization power spectra [15]. Even within ΛCDM, the Planck internal features drive a moderate tension between the low-multipoles ($\ell < 800$) and high-multipoles ($\ell > 800$) constraints [14]. In particular, the Planck TT $\ell > 800$ data favors higher fluctuation amplitude A_s and matter density $\Omega_m h^2$ compared to the lower multipole range, by about 3σ [14]. Even though the significance of any individual shift is reduced in the multi-dimensional parameter space, this disagreement drives the sizable differences in σ_8 and H_0 posteriors, which play a more significant role in a comparison with low-redshift cosmological probes. Moreover, in some extensions of the ΛCDM model the overly enhanced smoothing of the CMB acoustic peaks can strongly affect the parameter constraints. For instance, a non-minimal neutrino mass lowers the predicted lensing power compared to ΛCDM, leading to a surprisingly tight limit, $\sum m_\nu < 0.26\,\mathrm{eV}$ at the 95% confidence level (CL) [3]. If one marginalizes over the lensing information contained in the smoothing of the peaks of the CMB power spectra, the Planck constraint degrades to $\sum m_\nu < 0.87\,\mathrm{eV}$ at 95% CL [15]. In a cosmological model with extra relativistic degrees of freedom in the plasma, parameterized by an effective number of neutrinos N_{eff}, the arbitrary gravitational lensing opens up a new degeneracy direction between H_0 and N_{eff} parameters, opening an interesting avenue to reduce the H_0 tension [15]. Alternative CMB measurements, especially on small angular scales, can provide an important consistency check for the Planck results.

Small-scale CMB anisotropies can be probed by ground-based telescopes with exceptional precision. The most accurate measurements of the CMB temperature and polarization power spectra have been taken by the South Pole Telescope (SPT-3G) [16] and the Atacama Cosmology Telescope (ACT Data Release 4, ACT-DR4) [17]. Interestingly, these observations show no deviation from the standard lensing effect predicted by the baseline ΛCDM model. Since the ground-based experiments have a higher sensitivity to small scales, it is highly beneficial to combine the full-sky and ground-based CMB measurements in one cosmological analysis. Indeed, Ref. [18] showed that the Planck large-scale temperature data combined with the SPTpol polarization and lensing measurements within ΛCDM predict a substantially lower value of S_8, consistent with direct probes in the late Universe. This result suggests that the S_8 tension can be attributed to the excess smoothing of acoustic peaks in the Planck data that pulls the late-time amplitude to higher values. This CMB setup also alleviates the Hubble tension down

to 2.5σ statistical significance. The same methodology has been applied in the Early Dark Energy (EDE) scenario to investigate the cosmological tensions [19]. The combined-data approach yields parameter constraints with only modestly larger error bars compared to the baseline Planck analysis, see Refs. [18,19].

While the cosmological tensions can be partially explained by internal features in the Planck data, they may also constitute hints of new physics in the early and/or late Universe (for a review, see, e.g,. [1]). The class of late-time scenarios which invoke modifications in the dark energy sector has been extensively investigated in the literature [20–26]. These models assume variations in the dark energy equation of state parameter w_{DE}, and therefore in the dark energy density ρ_{DE}. Such cosmological scenarios typically resolve the Hubble tension within 2σ at the price of a phantom-like dark energy with $w_{\mathrm{DE}} < -1$. At the same time, model-independent studies based on reconstructions of late Universe point towards a possible phantom crossing in the dark energy equation of state, see, e.g., [27–31]. Moreover, a generic analytical approach [32] showed that simultaneously solving the H_0 and S_8 tensions necessarily requires $w_{\mathrm{DE}}(z)$ to cross the value $w_{\mathrm{DE}} = -1$ [33]. It is thus important to investigate the potential of dynamical dark energy models with phantom crossing when using alternative CMB measurements.

In this work, we revisit the combined data analysis [18] by incorporating newer SPT-3G polarization measurements. Specifically, we utilize the SPT-3G TE and EE power spectra, the SPTpol lensing reconstruction, and the Planck TT $\ell < 1000$ data. First, we validate the statistical agreement among the different CMB measurements in the ΛCDM model. Next, we explore two physically well-motivated extensions: ΛCDM with massive active neutrinos (ΛCDM$+\sum m_\nu$) and ΛCDM with extra relativistic degrees of freedom (ΛCDM$+N_{\mathrm{eff}}$). The main goal of this study is to obtain the alternative parameter constraints unaffected by the Planck lensing-like anomaly. In passing, we explore the potential of ΛCDM$+\sum m_\nu$ and ΛCDM$+N_{\mathrm{eff}}$ models to alleviate one or both cosmological tensions. Finally, we compare our results to those from the baseline Planck analysis.

We also explore the possibility of dynamical dark energy using two model-independent approaches. The first scenario, dubbed Phantom-crossing Dark Energy (PDE) [34], parameterizes the dark energy density $\rho_{\mathrm{DE}}(z)$ through a truncated Taylor series expansion. There is no assumption about the physical mechanism of dark energy except that it produces a phantom cross-

ing during the evolution of the Universe. It has been argued that PDE is capable of alleviating the tension between the early- and late-Universe determinations of H_0 [34]. The second scenario considered is the Transitional Dark Energy (TDE), originally suggested in [23]. This is a four-parameter dynamical dark energy model based on a phenomenological reconstruction of the effective dark energy equation of state, $w_{\mathrm{DE}}^{\mathrm{eff}}$, defined by $\rho_{\mathrm{DE}}(z) = \rho_{\mathrm{DE}}(0)(1+z)^{3(1+w_{\mathrm{DE}}^{\mathrm{eff}})}$ [35]. Ref. [23] argues that a sharp transition in $w_{\mathrm{DE}}^{\mathrm{eff}}$ at $1 < z < 2$ could simultaneously address the H_0 and S_8 tensions. We assess the potential of the PDE and TDE scenarios in resolving the cosmological tensions using the alternative CMB data combination along with large-scale structure and supernova measurements.

This work improves upon the previous analyses [18,19] in the following ways. First, we utilize the CMB polarization measurements from the SPT-3G instrument [16] which represent a significant advancement over previous SPTpol results [36]. Second, we perform a full-shape analysis of the BOSS DR12 galaxy data, including information from the power spectrum multipoles [37], the real-space power spectrum [38], the reconstructed power spectrum [39], and the bispectrum monopole [12]. We also consider multiple BAO measurements based on catalogs of emission-line galaxies, quasars, Lyα absorption, and cross-correlation between the last two, tracing the cosmological evolution back to earlier times. Third, we use the Pantheon supernova data to constrain the background cosmology in late-time modifications. Fourth, when including the SH0ES data, we adopt the full distance ladder approach rather than relying on the standard Gaussian constraint on H_0.

The outline of this paper is as follows. In Section 2 we describe our methodology and introduce all datasets used in the analysis. In Section 3 we briefly describe the main results. In Section 4 we validate our CMB setup. In Section 5 we present cosmological constraints in the ΛCDM scenario. In Section 6 we fit the parameters of ΛCDM$+\sum m_\nu$ and ΛCDM$+N_{\mathrm{eff}}$ models to cosmological data and compare our results with those in the Planck analysis. In Section 7 we examine the PDE scenario as a possible solution to the cosmological tensions. In Section 8 we conduct the same analysis for the TDE model. We present our conclusions in Section 9.

Six appendices contain supplementary materials. In Appendix A we assess the consistency between our CMB dataset and the Planck TT $\ell > 1000$ power spectrum. We also examine the sensitivity of our CMB-based parameter constraints to the choice of a Planck TT data cutoff. Appendix B estimates the expected

shifts in parameter constraints inferred from shared datasets. In Appendix C we illustrate the difference between the entire distance ladder approach and the traditional Gaussian constraint on H_0 in the PDE model. Appendix D presents the parameter constraints in the full Planck data analysis inside the PDE framework. In Appendix E we examine the sensitivity of parameter constraints to the choice of the TDE priors. Appendix F presents a complete breakdown of the best-fit $\chi^2_{\min}$ values per experiment for all models.

2. METHOD AND DATA

In this Section we describe our analysis procedure and datasets.

2.1. Method

We obtain cosmological parameter constraints using the modified Einstein–Boltzmann code `CLASS-PT` [40], interfaced with the `Montepython` Monte Carlo sampler [41, 42]. We perform the Markov Chain Monte Carlo (MCMC) analysis, sampling from the posterior distributions using the Metropolis-Hastings algorithm [43, 44]. The plots and marginalized constraints are generated with the latest version [2] of the `getdist` package [45].

In the ΛCDM model we vary the following set of cosmological parameters: ω_{cdm}, ω_b, H_0, $\ln(10^{10}A_s)$, n_s, τ, where H_0 is the Hubble constant, which can be recast as $H_0 \equiv h \times 100\,\mathrm{km\,s^{-1}\,Mpc^{-1}}$. Then $\omega_{cdm} \equiv \Omega_{cdm}h^2$, $\omega_b \equiv \Omega_b h^2$ with Ω_{cdm} and Ω_b standing for the relative contributions of cold dark matter and baryons to the present energy density of the Universe. A_s and n_s are the amplitude and tilt of the primordial spectrum of scalar perturbations, τ denotes the reionization optical depth. In ΛCDM we assume the normal neutrino hierarchy with the total active neutrino mass $\sum m_\nu = 0.06\,\mathrm{eV}$ and fix N_{eff} to the default value 3.046. Additionally, we vary $\sum m_\nu$ in the ΛCDM+$\sum m_\nu$ model and N_{eff} in the ΛCDM+N_{eff} model. In the ΛCDM+$\sum m_\nu$ model we approximate the neutrino sector with three degenerate massive states to boost the evaluation of the Einstein-Boltzmann code. In the PDE and TDE models we extend the dark energy sector as described in Secs. 7 and 8.

Throughout our analysis the Hubble parameter H_0 is measured in units of km·s^{-1}·Mpc^{-1}, the sum of neutrino masses $\sum m_\nu$ is in units of eV, the present size of the horizon at the drag epoch r_{drag} is in Mpc, the angular diameter distance $D_A \equiv 1/(1+z)\int_0^z dz'/H(z')$ is in km·s^{-1}·Mpc.

2.2. Data

Hereafter we describe the datasets involved in this analysis.

PlanckTT-lowℓ: We use the Planck `Plik` likelihood for the temperature (TT) power spectrum truncated at multipoles $30 \le \ell < 1000$. We combine it with the `Commander` TT data in the angular multipole range $2 \le \ell < 30$ [3].

SPT-3G: We utilize the SPT-3G measurements of the E-mode (EE) polarization power spectrum and the temperature-E (TE) cross-power spectrum produced during a four-month period in 2018 [16].

This data includes the six EE and TE cross-frequency power spectra over the angular multipole range $300 \le \ell < 3000$. Following the original analysis [16], we include modeling of polarized Galactic dust for TE and EE spectra and Poisson-distributed point sources in the EE power spectrum. The CMB theoretical spectra are modified in order to account for the effects of instrumental calibration, aberration, supersample lensing and survey geometry [3].

Lens: We use the measurement of the lensing potential power spectrum, $C_\ell^{\phi\phi}$, in the multipole range $100 < \ell < 2000$ from the SPTpol survey [46]. The lensing potential is reconstructed from a minimum-variance quadratic estimator that combines both the temperature and polarization CMB maps. We incorporate the effects of the survey geometry and correct the $C_\ell^{\phi\phi}$ for a difference between the fiducial cosmology assumed in the lensing reconstruction and the cosmology of the SPTpol patch following the procedure described in [46] [4].

We use a recent measurement of the reionization optical depth from Ref. [47]. We impose a Gaussian constraint,

$$\tau = 0.0581 \pm 0.0055\,, \tag{1}$$

determined from the Planck `SRoll2` polarization (EE) maps using the likelihood approximation scheme

---

[3] We made the SPT-3G likelihood for the Montepython environment publicly available at https://github.com/ksardase/SPT3G-montepython

[4] The SPTpol likelihood used in this analysis is publicly available at https://github.com/ksardase/SPTPol-montepython

momento [5]. We include the measurement (1) in all data analyses. We do not mention it in dataset names for brevity.

We combine all the CMB measurements above into one dataset that we call **Base**. To provide an additional test, we replace the Lens likelihood with the Planck lensing reconstruction from [3]. We refer to this combination as **Base′**.

Planck 2018: For the standard CMB analysis we use the official Planck TTTEEE+lensing and low-ℓ TT likelihoods [3]. Note that we do not include the large-scale polarization data from Planck, choosing instead to constrain the optical depth τ via the Gaussian prior (1), as described above. It allows us to perform a direct comparison with our baseline results.

LSS: We perform a full-shape analysis of the large-scale power spectrum and bispectrum of the BOSS DR12 galaxy data. The galaxies were observed in the North and South Galactic Caps (NGC and SGC, respectively). We divide each sample into two non-overlapping redshift slices, encompassing $0.2 < z < 0.5$ and $0.5 < z < 0.75$ (with effective redshifts 0.38 and 0.61), giving a total of four data chunks. We apply a window-free approach [48, 49] which allows us to measure the unwindowed power spectrum and bispectrum directly from the observational data. For every data chunk we analyze the following datasets: [6]

- *Redshift-Space Power Spectrum, P_ℓ:* We use the pre-reconstructed power spectrum monopole, quadrupole and hexadecapole in the range $k \in [0.01, 0.2]\,h\mathrm{Mpc}^{-1}$ with bin width $\Delta k = 0.005\,h\mathrm{Mpc}^{-1}$. Our data cuts are motivated by the results of Refs. [51, 52].

- *BAO parameters, $\alpha_{rec}^{\mathrm{DR12}}$:* We include the BAO measurements extracted from the post-reconstructed power spectra, as discussed in [39]. These are analyzed in combination with the unreconstructed spectra using a joint covariance matrix.

- *Real-Space Power Spectrum, Q_0:* We employ an analog to the real space power spectrum computed from the redshift-space multipoles via $Q_0(k) \equiv P_0(k) - \frac{1}{2}P_2(k) + \frac{3}{8}P_4(k)$ with $k \in [0.2, 0.4]\,h\mathrm{Mpc}^{-1}$. This statistic is used to mitigate the impact of fingers-of-God [38].

- *Bispectrum, B_0:* We include the bispectrum monopole in the range $k \in [0.01, 0.08]\,h\mathrm{Mpc}^{-1}$ with bin width $\Delta k = 0.01\,h\mathrm{Mpc}^{-1}$ following [12]. In total, 62 bispectrum bins are generated.

To model the above statistics, we utilize the effective field theory (EFT) of large scale structure as implemented in the CLASS-PT code [40]. For consistency, we compute the power spectrum and bispectrum up to one-loop and up to tree-level order in the cosmological perturbation theory respectively. Our analysis features a complete treatment of all necessary components: non-linear corrections, galaxy bias, ultraviolet counterterms (to consistently account for short-scale physics), infrared resummation (to treat long-wavelength displacements), and stochastic bias. We marginalize the posteriors over all relevant nuisance parameters for each data chunk along the lines of Ref. [12] [7]. Detailed information about the EFT theoretical model and nuisance parameters can be found in Ref. [40]. Our EFT-based analysis pipeline was validated on high-fidelity mock galaxy catalogs [37, 51–54].

We supplement the BOSS DR12 measurements described above with the following BAO data:

- 6dFGS at $z_{\mathrm{eff}} = 0.106$ [55]

- SDSS DR7 MGS at $z_{\mathrm{eff}} = 0.15$ [56]

- eBOSS quasar sample at $z_{\mathrm{eff}} = 1.48$ [57]

- Auto-correlation of Lyα absorption and its cross correlation with quasars at $z_{\mathrm{eff}} = 2.33$ from the final eBOSS data release [58]

- eBOSS emission line galaxy sample at $z_{\mathrm{eff}} = 0.845$ [59]. We do not include the full-shape measurements of emission line galaxies because their impact on the eventual parameter constraints is rather limited as shown in [60].

S_8: We consider the DES-Y3 photometric galaxy clustering, galaxy-galaxy lensing, and cosmic shear measurements [9], in addition to weak gravitational

---

[5] Note that the Planck 2018 legacy release High Frequency Instrument (HFI) polarization maps are based the SRoll1 map-making algorithm. The improved map-making algorithm SRoll2 significantly reduces large-scale polarization systematics compared to the SRoll1 processing [47]. This results in a 40% tighter constraint on τ compared to the Planck legacy release [3].

[6] The previous full-shape BOSS analyses were affected by an error in the public BOSS power spectra due to invalid approximation in the power spectrum normalization, for details see [50]. In the window-free approach we do not require modeling the mask, so our analysis is not affected by this problem.

[7] We assume physical priors on nuisance parameters from [12]. We have checked that our results are not affected by EFT priors, thanks to including the CMB data in our analysis.

lensing measurements from KiDS-1000 [10] and HSC [61]. We combine these results in the form of a Gaussian prior,

$$S_8 = 0.772 \pm 0.013 \,. \tag{2}$$

We treat this S_8 measurement separately from the other LSS data since it allows us to test the consistency of individual likelihoods before combining them into a single set.

SH0ES: We include the distance measurements of Type Ia supernovae in the Hubble flow calibrated with local geometric anchors via the Cepheid period luminosity relation. We utilize the local distance ladder approach as implemented in the `distanceladder` package [8] [62]. To match the SH0ES methodology, we set the upper redshift cut at $z = 0.15$ for the supernova sample. The `distanceladder` implementation using Cepheid calibration yields an absolute magnitude of Type Ia supernova [62],

$$M_B = -19.226 \pm 0.039 \,, \tag{3}$$

which closely reproduces the SH0ES result [63]. Assuming ΛCDM cosmology, the Cepheid calibration recovers an accurate mean value of H_0 with respect to the SH0ES result [2],

$$H_0 = 73.2 \pm 1.3 \,\mathrm{km \cdot s^{-1} \cdot Mpc^{-1}} \,. \tag{4}$$

SN: We eventually use the luminosity distance data of 1048 type Ia supernovae from the Pantheon catalog [64]. Since the Pantheon supernova calibration produced by CMB is not compatible with the SH0ES calibration, we do not combine the SN, SH0ES and CMB data in our analysis.

3. SUMMARY OF OUR MAIN RESULTS

Let us briefly summarize our main results before going into the technical details. We fit the model parameters to the cosmological data in five different cosmological scenarios: ΛCDM, ΛCDM+$\sum m_\nu$, ΛCDM+N_eff, PDE and TDE.

Figure 1 shows our main results in the ΛCDM+$\sum m_\nu$ model. The Base dataset yields a substantially weaker constraint on $\sum m_\nu$ compared to the full Planck analysis. The high-ℓ temperature spectrum in the Planck 2018 data favors more lensing than is allowed in ΛCDM, strengthening the limit on
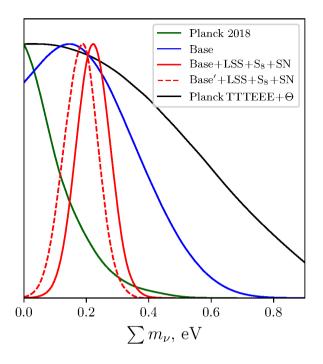
[8] https://github.com/kylargreene/distanceladder

Fig. 1. Marginalized 1d posterior distributions of $\sum m_\nu$ for the Planck 2018 (green), Base (blue), Base+LSS+S_8+SN (red), Base′+LSS+S_8+SN (dashed red) and Planck TTTEEE+Θ (black) analyses. The Base′ includes the Planck lensing reconstruction from Ref. [3]. Planck TTTEEE + Θ refers to the result after marginalizing over lensing information in the CMB maps from Ref. [15]

the total neutrino mass [3]. The Base + LSS + S_8 + SN dataset provides a 4.1σ evidence of non-zero neutrino masses, $\sum m_\nu = 0.221 \pm 0.055$ eV. Using the Planck measurement of the lensing-potential power spectrum we infer a consistent estimate $\sum m_\nu = 0.176 \pm 0.056$ eV. The LSS data contribute to the neutrino mass measurements by breaking the CMB degeneracies between $\sum m_\nu$ and other cosmological parameters. We also display the Planck limit after marginalizing over the lensing information in the CMB power spectra [15]. This illustrates the amount of information encoded in the Planck gravitational lensing.

Figure 2 summarizes the H_0 and S_8 constraints in different models. In all scenarios our analysis yields systematically lower values of S_8 being in good agreement with the low-redshift cosmological probes (2). Note that the Planck 2018 data exhibits the S_8 tension at the 3.3σ significance level. In ΛCDM the Base analysis predicts a moderately higher value of H_0 alleviating the Hubble tension to a 2.7σ level. The Base+LSS+S_8+SN data shrinks the error bars on H_0 and S_8 in half. The
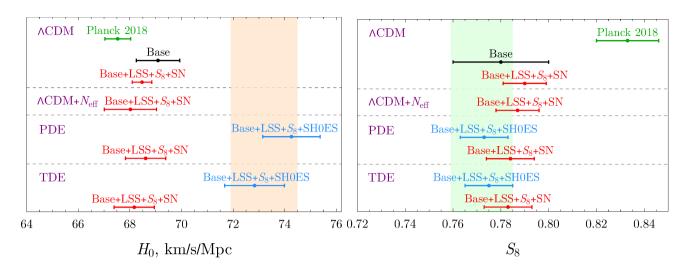
Fig. 2. Estimates (mean value with 1σ error bar) of the Hubble constant H_0 (left panel) and the late-time amplitude $S_8 \equiv \sigma_8 \sqrt{\Omega_m/0.3}$ (right panel) in the ΛCDM, ΛCDM+N_{eff}, PDE and TDE models. The orange band represents the direct measurement of H_0 (4) reported by SH0ES, whereas the green band shows a combined constraint on S_8 (2) coming from the photometric surveys DES-Y3, KiDS-1000 and HSC (both are given at 68% CL)

ΛCDM+N_{eff} model partially alleviates the Hubble tension at the cost of inflating the error on H_0. The late-time scenarios (PDE and TDE), which drastically modify the dark energy sector, open a path towards combining CMB with the SH0ES data. In both models, the Base + LSS + S_8 + SH0ES dataset yields significantly higher values of H_0 consistent with SH0ES. However, the Base + LSS + S_8 + SN combination suggests a systematically lower H_0 in a moderate ($\sim 3\sigma$) tension with the SH0ES constraint (4). The difference in the H_0 recovery reflects the tension between the SN calibration produced by CMB+BAO and the local astrophysical calibration by Cepheids.

We conclude that the H_0 tension cannot be resolved by non-trivial dynamics in the dark energy sector when all data are taken into account. Our results reinforce the previous analyses [25, 65–68] which show through the late Universe reconstruction that CMB, BAO and SN data do not allow for high H_0 values.

4. CMB SETUP VALIDATION

Our main CMB combination dubbed Base includes the Planck TT power spectrum in the multipole range $2 \leq \ell < 1000$, the TE and EE spectra over $300 \leq \ell < 3000$ from the SPT-3G data, and the power spectrum of the lensing potential at $100 < \ell < 2000$ measured by the SPTpol survey. We ignore the correlation between 2- and 4-point functions as it has been shown to be negligible at current sensitivities [69, 70].

This upgrades the CMB setup used in the previous analysis [18] by featuring the updated SPT-3G polarization measurements.

First, we test the consistency of our CMB setup at the level of the spectra. We fit the Base data within ΛCDM by varying all cosmological and nuisance parameters along the lines of Sec. 2.1. Figure 3 shows the Planck TT, SPT-3G TE and EE residuals with respect to the reference ΛCDM best-fit model of the Base data. To improve readability, we show the Planck TT power spectrum in the bands of width $\Delta\ell \approx 31$ from the `Plik_lite` likelihood [3]. As far as the SPT-3G data is concerned, we display the minimum-variance TE and EE bandpowers with the error bars corresponding to the diagonal elements of the bandpower covariance matrix (which does not include beam and calibration uncertainties [16]). We show the CMB residuals in units of σ_{CV}, the cosmic variance error per multipole moment, defined as

$$\sigma_{\mathrm{CV}} = \begin{cases} \sqrt{\dfrac{2}{2\ell+1}} C_\ell^{TT}, & \text{TT}, \\[2mm] \sqrt{\dfrac{1}{2\ell+1}} \sqrt{C_\ell^{TT} C_\ell^{EE} + (C_\ell^{TE})^2}, & \text{TE}, \\[2mm] \sqrt{\dfrac{2}{2\ell+1}} C_\ell^{EE}, & \text{EE}. \end{cases} \quad (5)$$

We found that our reference ΛCDM model matches both the Planck TT data in the range $30 \leq \ell < 1000$ and the SPT-3G TE and EE measurements (across the entire multipole range) within statistical uncertainties. We detect the oscillatory residuals in the temperature power spectrum at $\ell > 1000$ which cannot be captured
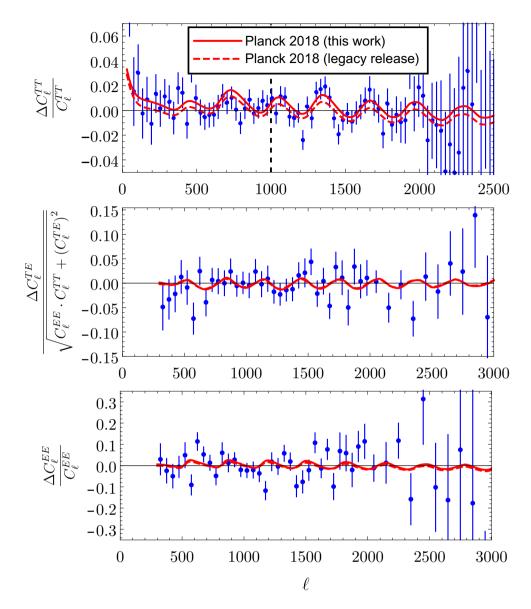
Fig. 3. CMB residuals of the Planck TT (top panel), SPT-3G TE (middle panel) and EE (bottom panel) data with respect to the reference ΛCDM best-fit model of the Base likelihood (blue points). The red line corresponds to the difference between the ΛCDM best-fit model for the full Planck 2018 likelihood and the reference ΛCDM model (this work). The dashed red line is the same for the official Planck best-fit model [3] (legacy release). The dashed black line flags the maximum multipole $\ell = 1000$ used when fitting the reference ΛCDM model

by our best-fit estimate. The associated difference is attributed to an extra peak-smoothing effect observed in the Planck high-ℓ TT data. The residuals are not obviously anomalous being always within a 1.5σ statistical uncertainty, however they represent an oscillatory pattern across the broad range of angular scales which can impact the parameter constraints, for detail see [14, 71]. When fitting the entire Planck 2018 spectra (red line), the best-fit model restores an agreement with the Planck high-ℓ TT data. This is achieved at

the cost of a shift in cosmological parameters, mainly A_s and ω_{cdm} which are pulled up by around 2σ [3]. At the same time, the Planck 2018 estimate slightly deteriorates the fit to the PlanckTT-lowℓ data compared to the reference ΛCDM model. This shows that the oscillatory residual in the Planck TT data has a moderate impact on cosmological parameters within the ΛCDM model. In extended cosmologies, the Planck internal features can introduce larger shifts in the parameter constraints.

It is important to elucidate the difference between our Planck 2018 analysis and the Planck legacy release which uses the low-ℓ EE likelihood. To that end, in Fig. 3 we show the residuals of the official Planck best-fit model [3] with respect to the reference ΛCDM estimate (dashed red line). Our results demonstrate good agreement between the two Planck results. The Planck 2018 analysis implies a $\sim 10\%$ higher τ compared to that in the legacy release. This leads to a 1σ upward shift in A_s which increases lensing smoothing and, therefore, provides a better fit to the Planck TT data at $\ell > 1000$. The Planck 2018 model also features a 0.6σ higher value of $A_s e^{-2\tau}$ that causes a positive shift in the C_ℓ^{TT} at large scales. While the two Planck analyses yield the consistent results, we choose to use the Planck 2018 data to be in line with the τ measurement (1) used in the Base combination.

In order to assess consistency of our CMB setup, we perform a χ^2 test for each individual likelihood. Table 1 presents the χ^2_{min} values for the best-fit ΛCDM models to the Planck 2018 and Base data as well as the associated number of degrees of freedom, N_{dof}. Since the constraints on nuisance parameters for both Planck and SPT-3G data are dominated by their priors, we only account for the 5 free ΛCDM parameters.

The Base data approach improves the χ^2 statistic for all CMB likelihoods with respect to the Planck 2018 analysis. The most significant contribution originates from the SPT-3G bandpowers which give $\Delta\chi^2_{\mathrm{SPT\text{-}3G}} = -8.05$. The Base analysis also improves the fit to the PlanckTT-lowℓ data and the CMB lensing though the corresponding improvement is modest given a large number of the degrees of freedom N_{dof}. In total, the cumulative χ^2_{min} in the Base data approach improves by $\Delta\chi^2_{\mathrm{tot}} = -17.18$ relative to the Planck 2018 analysis. Our results demonstrate that the Base combination is mutually consistent and can be used in cosmological analyses.

We found that the Base data and the Planck TT $\ell > 1000$ power spectrum are in a mild (2.4σ) tension when analyzing the shifts in the full parameter space (see Appendix A) [9]. Note that the two individual cosmological parameters, ω_{cdm} and H_0, which play a significant role in comparisons with low-redshift cosmological probes, differ by 3σ. As discussed before, this disagreement is mainly caused by the oscillatory residual in the Planck TT spectrum that pulls σ_8 and

---

[9] Noteworthy, the Planck TT $\ell < 1000$ and $\ell > 1000$ data are consistent at the level of $1.6 - 1.8\sigma$ [14, 71] which justifies the combination of these measurements in one dataset.

ω_{cdm} to higher values. For this reason, we do not combine the Base and the Planck TT $\ell > 1000$ spectrum into one dataset.

Our PlanckTT-lowℓ likelihood can be viewed as an emulation of the WMAP measurements. Indeed, the WMAP-9 and Planck TT data agree very closely at the level of the CMB power spectrum across $\ell < 1000$ (see Fig. 48 in Ref. [72]). As the WMAP temperature maps reach the signal-to-noise ratio of unity by $\ell_{\mathrm{max}} \simeq 600$ [14], the Planck TT $\ell < 600$ data serves as a proxy of the WMAP measurements. In Appendix A we examine the sensitivity of our parameter constraints to the choice of a Planck TT data cutoff, $\ell_{\mathrm{max}}^{\mathrm{TT}}$, and find nearly indistinguishable results for $\ell_{\mathrm{max}}^{\mathrm{TT}} = 600$ and $\ell_{\mathrm{max}}^{\mathrm{TT}} = 1000$. Thus, the PlanckTT-low$\ell$ data used in this work can be seen as a proxy for WMAP.

5. ΛCDM MODEL

In this section we present the parameter measurements in the ΛCDM model. First, we scrutinize the cosmological inference from the Base dataset. Second, we present the parameter constraints using the large-scale structure and supernova data.

5.1. Base data

To assess the information gain coming from individual experiments we explore the parameter constraints from the SPT and Planck data separately. Figure 4 shows the two-dimensional (2d) posterior distributions for various dataset combinations. The corresponding one-dimensional (1d) marginalized parameter constraints are tabulated in Tab. 2.

Let us start with the SPT-3G data. Our parameter estimates agree with those from the SPT-3G official release [16] at the precision level of 0.1σ in terms of the statistical error, which can be explained by the use of a different Gaussian constraint on τ in Ref. [16]. These measurements significantly improve upon the previous results from the SPTpol survey [36]. The parameter constraints are also competitive with those from other modern ground-based experiments [17].

Next, we combine the SPT-3G data with the Lens measurement. Adding information on the lensing potential power spectrum significantly shrinks the error bars on cosmological parameters. In particular, the H_0 and σ_8 measurements improve by 20% and 30%, re-

Table 1. $\chi^2_{\min}$ values for the ΛCDM best-fit models to the Planck 2018 (second column) and Base (third column) data. The τ-prior is set by (1). N_{dof} gives the number of degrees of freedom equal to the difference between the number of data points and the number of model parameters adjusted to produce the best-fit theory curve

ΛCDM	Planck 2018	Base	N_{dof}
SPT-3G	530.36	522.31	523
Planck TT, $\ell < 30$	23.22	21.15	28
Planck TT, $30 \le \ell < 1000$	410.45	406.05	444
Lens	7.93	5.57	10
τ-prior	0.31	0.01	1
Total $\chi^2_{\min}$	972.27	955.09	1006

Table 2. Marginalized 1d constraints on cosmological parameters in the standard ΛCDM model for four datasets. Recall that the Base dataset includes SPT-3G+Lens+PlanckTT-lowℓ

	ΛCDM			
Parameter	SPT-3G	SPT-3G+Lens	PlanckTT-lowℓ	Base
$100\,\omega_b$	2.243 ± 0.033	2.239 ± 0.033	2.264 ± 0.039	2.255 ± 0.020
$10\,\omega_{cdm}$	1.147 ± 0.036	1.162 ± 0.029	1.141 ± 0.032	1.151 ± 0.018
H_0	68.98 ± 1.51	68.36 ± 1.20	69.87 ± 1.68	69.09 ± 0.84
τ	0.058 ± 0.006	0.058 ± 0.006	0.058 ± 0.006	0.058 ± 0.005
$\ln(10^{10}A_s)$	3.016 ± 0.023	3.022 ± 0.018	3.035 ± 0.014	3.036 ± 0.012
n_s	1.004 ± 0.019	1.001 ± 0.017	0.979 ± 0.011	0.977 ± 0.006
r_{drag}	148.47 ± 0.98	148.10 ± 0.76	148.38 ± 0.59	148.18 ± 0.43
Ω_m	0.290 ± 0.020	0.298 ± 0.016	0.282 ± 0.019	0.290 ± 0.010
σ_8	0.791 ± 0.016	0.798 ± 0.011	0.789 ± 0.013	0.793 ± 0.008
S_8	0.778 ± 0.041	0.796 ± 0.030	0.766 ± 0.038	0.780 ± 0.020

spectively, upon including the Lens data. Overall, the parameters constraints are compatible with those from the SPT-3G analysis in agreement with [73].

As a next step, we examine the cosmological inference from the PlanckTT-lowℓ data. We found that the parameter constraints are highly competitive with those from the SPT-3G+Lens analysis. In particular, the SPT-3G+Lens combination imposes tighter constraints on ω_b, ω_c, H_0 and σ_8 parameters whereas the PlanckTT-lowℓ data provides more stringent bounds on $\ln(10^{10}A_s)$ and n_s. Thus, the two datasets naturally complement each other, and combining them at the likelihood level will yield a significant information gain.

We combine the Planck and SPT measurements into one dataset (Base). Indeed, the parameter constraints significantly improve upon those inferred from the SPT-3G+Lens and PlanckTT-lowℓ data separately. In particular, the error bars on H_0 and S_8 shrink by 50% compared to that in the PlanckTT-lowℓ analysis, namely

$$S_8 = 0.780 \pm 0.020,$$
$$H_0 = 69.09 \pm 0.84 \, \mathrm{km \cdot s^{-1} \cdot Mpc^{-1}}. \tag{6}$$

Our constraint on S_8 is perfectly consistent with the direct measurements (2). In turn, the statistical difference between the CMB-based estimate of H_0 and the local measurement of this parameter (4) reported by the SH0ES collaboration decreases from 4.2σ to 2.7σ level. Thus, the Hubble tension reduces compared to that if one would use the full Planck likelihood but still remains statistically implausible. We will examine the remaining tension in extended cosmologies in the following sections.

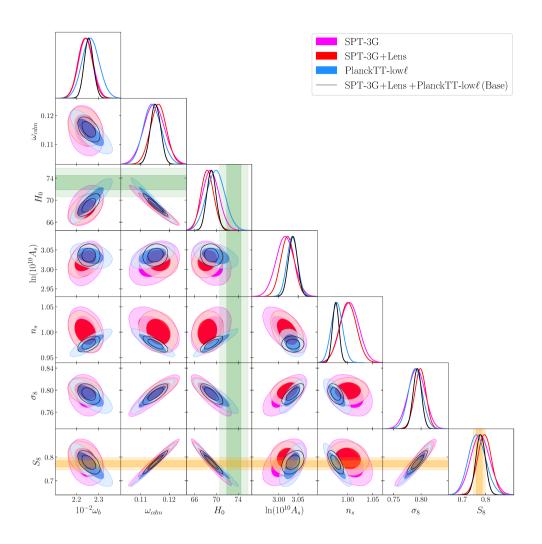It is instructive to compare our results with those of the previous work [18] that used the PlanckTT-lowℓ

Fig. 4. Marginalized 2d posterior distributions of the cosmological parameters in the ΛCDM model for SPT-3G (magenta), SPT-3G+Lens (red), PlanckTT-lowℓ (blue), combined SPT-3G+Lens+PlanckTT-lowℓ (black) datasets. The Gaussian prior on τ (1) is always adopted. The yellow bands represent 1σ and 2σ constraints on S_8 (2) coming from the photometric surveys (DES-Y3, KiDS, HSC), whereas the green bands refer to the H_0 measurement (4) reported by the SH0ES collaboration

data along with the SPTpol polarization and lensing measurements. Our analysis predicts 1σ higher values of σ_8 and S_8 compared to the previous research. This effect is attributed to the latest SPT-3G data which favors higher values of the late-time fluctuation amplitude [16]. Overall, our analysis improves cosmological constraints by $10-20\%$ over that in Ref. [18].

5.2. Full data

Let us compare our CMB-based parameter constraints with those in the full Planck analysis. The 1d marginalized constraints on cosmological parameters are listed in Tab. 3. The resulting 2d posterior

distributions for different datasets are shown in Fig. 5.

The full Planck approach and the Base data lead to considerably different posterior distributions. Namely, the shifts in the posterior means between the Base and Planck 2018 analyses are

$$\Delta\omega_b = 0.6\sigma, \quad \Delta\omega_{cdm} = -2.2\sigma,$$

$$\Delta H_0 = 1.6\sigma, \quad \Delta\ln(10^{10}A_s) = -1.2\sigma, \qquad (7)$$

$$\Delta n_s = 1.4\sigma, \quad \Delta\sigma_8 = -2.3\sigma,$$

expressed in units of the posterior error of the two experiments combined in quadrature. This is a conservative estimate since the Planck 2018 and Base datasets

Table 3. Parameter constraints in the standard ΛCDM model with 1σ errors. The Gaussian prior on τ (1) is adopted. The Base dataset includes SPT-3G+Lens+PlanckTT-lowℓ

Parameter	ΛCDM				
	Planck 2018	Base	Base+LSS	Base+LSS $+S_8$	Base+LSS $+S_8+SN$
$100\,\omega_b$	2.241 ± 0.015	2.255 ± 0.020	2.240 ± 0.018	2.247 ± 0.018	2.245 ± 0.018
$10\,\omega_{cdm}$	1.197 ± 0.011	1.151 ± 0.018	1.174 ± 0.010	1.163 ± 0.008	1.163 ± 0.008
H_0	67.53 ± 0.50	69.09 ± 0.84	68.01 ± 0.46	68.49 ± 0.38	68.47 ± 0.38
τ	0.060 ± 0.005	0.058 ± 0.005	0.055 ± 0.005	0.053 ± 0.005	0.053 ± 0.005
$\ln(10^{10}A_s)$	3.055 ± 0.011	3.036 ± 0.012	3.034 ± 0.012	3.028 ± 0.011	3.027 ± 0.011
n_s	0.967 ± 0.004	0.977 ± 0.006	0.971 ± 0.005	0.973 ± 0.005	0.973 ± 0.005
$r_{\rm drag}$	147.12 ± 0.25	148.18 ± 0.43	147.75 ± 0.31	147.98 ± 0.28	147.97 ± 0.28
Ω_m	0.313 ± 0.007	0.290 ± 0.010	0.304 ± 0.006	0.297 ± 0.005	0.298 ± 0.005
σ_8	0.815 ± 0.005	0.793 ± 0.008	0.799 ± 0.006	0.793 ± 0.005	0.793 ± 0.005
S_8	0.833 ± 0.013	0.780 ± 0.020	0.803 ± 0.012	0.789 ± 0.009	0.790 ± 0.009

are not independent, sharing the common Planck TT $\ell < 1000$ likelihood and the τ measurement (1), see Appendix B. Although the cosmological constraints in these two CMB analyses are not obviously discrepant, the Planck 2018 data reveals more significant tensions with the low-redshift cosmological probes. Specifically, the CMB analysis based on the full Planck likelihood demonstrates the S_8 tension at the level of 3.3σ. This effect can be attributed to the overly enhanced smoothing of the acoustic peaks in the Planck data pulling the late-time fluctuation amplitude σ_8 and the physical density of dark matter ω_{cdm} to higher values, which results in a larger S_8. The Base combination features the Planck TT data over $\ell < 1000$, so our analysis is insensitive to the oscillatory residual in the Planck TT spectrum. The H_0 constraint inferred from the Planck 2018 data is also in a 4.2σ tension with the SH0ES measurement. A significantly lower value of H_0 in the full Planck analysis can be explained by an anti-correlation between σ_8 and H_0 parameters present in the CMB data as shown in Fig. 5, see also Ref. [3].

Next, we perform a joint analysis of the Base CMB data and the LSS likelihood (without S_8). The accuracy of cosmological constraints drastically improves upon including the LSS information. In particular, the LSS data brings a twice more accurate measurement of ω_{cdm}. This effect is attributed to the full-shape BOSS measurements which primarily constrain this parameter. The LSS data also shrinks the error bars on H_0 and S_8 by 45% and 40%, respectively, when compared with the Base only results. This leads to a more severe

3.8σ tension with the SH0ES constraint. Remarkably, the Base+LSS data analysis is consistent with the direct probes of S_8 at the 1.7σ level. It justifies further account for the S_8 data.

On the next step, we add the data on weak lensing and photometric galaxy clustering in the form of the Gaussian constraint on S_8 (2). We emphasize that the mean value of S_8 changes only by 1.1σ upon including the S_8 information. This illustrates a good agreement between the Base+LSS and S_8 datasets. Interestingly, the mean value of H_0 raises up by 1σ that slightly alleviates the Hubble tension down to 3.5σ level, cf. with (4).

Finally, we add the supernova data. We found that the parameter constraints upon including the SN data remain essentially unchanged. This result can be understood as follows. In ΛCDM the supernova sample mainly constrains Ω_m, which leads to $\Omega_m = 0.298 \pm 0.022$ [64]. However, our Base+LSS+S_8 data imposes a much tighter constraint on this parameter, $\Omega_m = 0.297 \pm 0.005$, which is mainly driven by the CMB and BOSS measurements. Thus, the SN data has very little constraining power when compared with the Base+LSS+S_8 combination. Our final constraints inferred from the Base+LSS+S_8+SN data read

$$S_8 = 0.790 \pm 0.009,$$
$$H_0 = 68.47 \pm 0.38\,{\rm km\cdot s^{-1}\cdot Mpc^{-1}}. \tag{8}$$

Our results demonstrate good agreement with the direct measurements of S_8 (at 1.1σ level). The Hubble tension persists at the 3.5σ level.
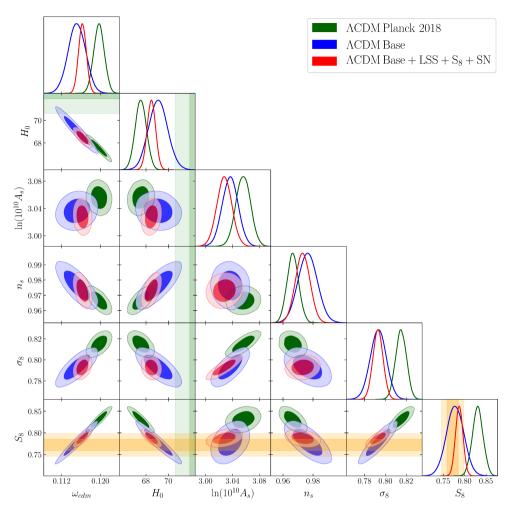
Fig. 5. Marginalized 2d posterior distributions of the cosmological parameters in the ΛCDM model for Planck 2018 (green), Base (blue) and Base $+$ LSS $+$ S$_8$ $+$ SN (red) datasets. The Gaussian prior on τ (1) is always set. The yellow bands represent 1σ and 2σ constraints on S_8 (2) coming from the photometric surveys (DES-Y3, KiDS, HSC), whereas the green bands refer to the H_0 measurement (4) reported by the SH0ES collaboration

As a comparison, we assess the minimal shifts in the posteriors means inferred from the Base+LSS+S$_8$+SN and Planck 2018 datasets,

$$\Delta\omega_b = 0.2\sigma, \quad \Delta\omega_{cdm} = -2.5\sigma,$$
$$\Delta H_0 = 1.5\sigma, \quad \Delta\ln(10^{10}A_s) = -1.8\sigma, \qquad (9)$$
$$\Delta n_s = 0.9\sigma, \quad \Delta\sigma_8 = -3.1\sigma.$$

Our approach predicts considerably smaller ω_{cdm} and σ_8 that pulls the S_8 value into consistency with the low-redshift probes (2). To a lesser extent, our CMB setup alleviates the H_0 tension. Interestingly, the shifts in ω_{cdm}, $\ln(10^{10}A_s)$ and σ_8 parameters have amplified compared to that inferred from the Base and Planck 2018 data, cf. with (7). Thus, the large-scale structure and supernova data support the cosmological inference based on the Base data.

6. MINIMAL EXTENSIONS OF THE BASE-ΛCDM MODEL

6.1. ΛCDM+$\sum m_\nu$

We start with the ΛCDM+$\sum m_\nu$ scenario. Table 4 presents the 1d marginalized constraints on cosmological parameters in the ΛCDM+$\sum m_\nu$ model. Figure 6 displays the 2d posterior distributions for different analyses.

Let us underline the main differences between our approach and the full Planck analysis. First, the Base data predicts a 2.2σ lower value of S_8 when compared with the Planck 2018 result. This makes our analysis entirely consistent with the low-redshift probes of S_8, whereas the full Planck approach is in a 3.3σ tension with the S_8 data (2). Second, the H_0 measure-

Table 4. Parameter constraints in the standard $\Lambda\text{CDM}+\sum m_\nu$ model with 1σ errors. The upper limits on neutrino masses are given at 95% CL. Recall, the Base dataset includes SPT-3G+Lens+PlanckTT-lowℓ

Parameter	$\Lambda\text{CDM}+\sum m_\nu$				
	Planck 2018	Base	Base+LSS	Base+LSS $+S_8$	Base+LSS $+S_8+$SN
$100\,\omega_b$	2.239 ± 0.015	2.246 ± 0.022	2.246 ± 0.018	2.247 ± 0.018	2.248 ± 0.018
$10\,\omega_{cdm}$	1.200 ± 0.013	1.163 ± 0.021	1.162 ± 0.012	1.159 ± 0.008	1.159 ± 0.008
H_0	$67.03^{+1.47}_{-0.71}$	$67.02^{+2.54}_{-1.61}$	67.15 ± 0.59	67.15 ± 0.60	67.25 ± 0.58
τ	0.060 ± 0.005	0.058 ± 0.005	0.057 ± 0.005	0.057 ± 0.005	0.057 ± 0.005
$\ln(10^{10}A_s)$	3.057 ± 0.011	3.040 ± 0.012	3.037 ± 0.012	3.037 ± 0.012	3.037 ± 0.011
n_s	0.966 ± 0.004	0.973 ± 0.007	0.974 ± 0.005	0.975 ± 0.005	0.975 ± 0.005
$\sum m_\nu$	< 0.30	< 0.513	0.221 ± 0.070	0.230 ± 0.057	0.221 ± 0.055
r_drag	147.07 ± 0.28	147.93 ± 0.49	147.98 ± 0.34	148.03 ± 0.28	148.05 ± 0.28
Ω_m	0.320 ± 0.016	0.316 ± 0.027	0.313 ± 0.007	0.313 ± 0.007	0.311 ± 0.007
σ_8	0.806 ± 0.019	0.760 ± 0.031	0.761 ± 0.018	0.758 ± 0.013	0.760 ± 0.013
S_8	0.832 ± 0.013	0.778 ± 0.021	0.777 ± 0.018	0.774 ± 0.010	0.773 ± 0.010

ments in the two analyses agree, but the Base data produces a two times larger error. Finally, we obtain the CMB-based constraint on the total neutrino mass, $\sum m_\nu < 0.513$ eV at 95% CL. This limit is considerably weaker than the Planck 2018 result, even though our Planck 2018 limit on the total neutrino mass is somewhat weaker than the Planck legacy release constraint, $\sum m_\nu < 0.24$ eV at 95% CL [3], due to the adoption of the Gaussian prior on τ (1) instead of large-scale polarization data. The main reason is the increased smoothing of the Planck TT power spectrum peaks and troughs at $\ell > 1000$ which strengthens the Planck 2018 constraint on the neutrino mass [3,15].

It is interesting to compare our Base limit on the neutrino mass with the results of the other CMB analyses which are insensitive to the lensing-induced smoothing of the acoustic peaks. First, one can marginalize over the lensing information that removes any effect of the peak smoothing in the CMB power spectra on cosmological parameter constraints. When allowing for arbitrary gravitational lensing in the Planck TT,TE,EE maps, the constraint on the total neutrino mass reads $\sum m_\nu < 0.87$ eV at 95% CL [15] [10]. Second, the combination of the Planck measurement of the CMB acoustic

scale (θ_*), the CMB lensing reconstruction power spectrum and BAO data leads to the limit $\sum m_\nu < 0.60$ eV at 95% CL [3] which is almost independent of lensing effects in the CMB spectra. Both measurements agree with the neutrino mass constraint inferred from the Base data. The Base analysis yields the considerably tighter bound due to the SPT-3G data which independently constrains $\sum m_\nu$ through the lensing-induced smoothing of CMB acoustic peaks.

The LSS data tremendously (by more than a factor of 3) improves the accuracy of H_0 recovery. This effect is driven by the distance information encoded in the BOSS galaxy spectra and anisotropic BAO measurements at intermediate redshifts. The LSS data significantly shrinks the error bars on other cosmological parameters, with the exception of $\ln(10^{10}A_s)$, which is primarily constrained by CMB, and τ, governed by (1). Our analysis does not feature data on weak lensing and photometric galaxy clustering, but its result is perfectly consistent with direct probes of S_8. Intriguingly, we find a 3.1σ evidence for non-zero neutrino masses, namely $\sum m_\nu = 0.221 \pm 0.070$ eV. The LSS data helps to break the CMB degeneracies between the $\sum m_\nu$ and the cosmological parameters, which significantly tightens the neutrino mass constraint.

Next, we add the S_8 data. As expected, including S_8 information substantially improves the bounds on σ_8 and S_8 parameters. It also tightens the ω_{cdm} constraint as this parameter largely controls the growth rate of cosmological matter perturbations. Striking, the limit on $\sum m_\nu$ remains essentially intact. This indicates that

---

[10] The method applied in [15] allows one to constrain the lensing potential power spectrum in a model independent way by modeling the principal components of the gravitational lensing potential. It should be contrasted with the standard approach of introducing a phenomenological parameter A_L which scales $C_\ell^{\phi\phi}$ at each point of the parameter space and cannot be interpreted in terms of the lensing potential [74].
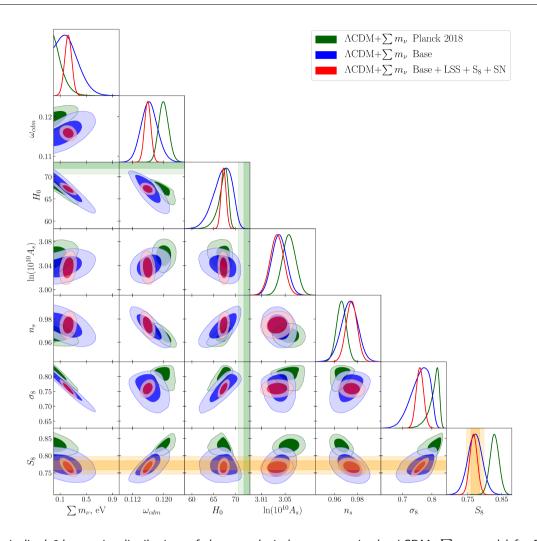
Fig. 6. Marginalized 2d posterior distributions of the cosmological parameters in the $\Lambda\text{CDM}+\sum m_\nu$ model for Planck 2018 (green), Base (blue) and Base + LSS + S_8 + SN (red) datasets. The Gaussian prior on τ (1) is imposed. The yellow bands represent 1σ and 2σ constraints on S_8 (2) coming from the photometric surveys (DES-Y3, KiDS, HSC), whereas the green bands refer to the H_0 measurement (4) reported by the SH0ES collaboration

the information on neutrino masses comes from breaking the degeneracies between the LSS and CMB rather than from the direct measurements of the late-time parameter S_8. All other constraints only barely change that demonstrates an excellent agreement between the Base + LSS and S_8 datasets.

Finally, we include the supernova data. We find that the parameter constraints remain virtually unchanged. The reason is the same as in the ΛCDM scenario: the background evolution is tightly constrained by CMB and LSS measurements, so the gain from adding the SN data is very modest. The Base + LSS + S_8 + SN analysis suggests the 4.1σ preference for non-zero $\sum m_\nu$ leading to

$$\sum m_\nu = 0.221 \pm 0.055 \text{ eV}. \qquad (10)$$

This estimate is consistent with both neutrino mass hierarchies. We emphasize that the information gain comes from the breaking of various degeneracies between LSS and CMB data and not from the S_8 constraint (2). In the full Planck data approach, the extra smoothing of CMB acoustic peaks strengthens the constraints on neutrino masses, making higher values of $\sum m_\nu$ implausible [3]. To validate the robustness of our result, we consider the Base′ + LSS + S_8 data which features the Planck lensing reconstruction [3]. This analysis yields $\sum m_\nu = 0.176 \pm 0.056$ eV which implies a non-zero neutrino mass at the 3.1σ level.

It is interesting to compare our results with those from Ref. [75] which analyzes the SPT-3G and ACT-

Table 5. The $\Delta\chi^2_{\min}$ and ΔAIC values between the best-fit ΛCDM$+\sum m_\nu$ and ΛCDM models to different datasets

Parameter	Base	Base+LSS	Base+LSS +S$_8$	Base+LSS +S$_8$+SN
$\Delta\chi^2_{\min}$	-1.22	-4.37	-6.22	-5.91
ΔAIC	$+0.78$	-2.37	-4.22	-3.91

Table 6. Parameter constraints in the ΛCDM$+N_{\text{eff}}$ model with 1σ errors. Recall, the Base dataset includes SPT-3G+Lens+PlanckTT-lowℓ

	ΛCDM$+N_{\text{eff}}$				
Parameter	Planck 2018	Base	Base+LSS	Base+LSS +S$_8$	Base+LSS +S$_8$+SN
$100\,\omega_b$	2.227 ± 0.021	2.263 ± 0.029	2.236 ± 0.021	2.237 ± 0.021	2.244 ± 0.021
$10\,\omega_{cdm}$	1.172 ± 0.029	1.168 ± 0.042	1.161 ± 0.037	1.138 ± 0.033	1.150 ± 0.030
H_0	66.38 ± 1.35	70.00 ± 2.37	67.52 ± 1.36	67.47 ± 1.36	$68.02^{+0.94}_{-1.08}$
τ	0.059 ± 0.005	0.058 ± 0.005	0.055 ± 0.005	0.054 ± 0.005	0.053 ± 0.005
$\ln(10^{10}A_s)$	3.048 ± 0.014	3.040 ± 0.016	3.030 ± 0.014	3.022 ± 0.013	3.025 ± 0.013
n_s	0.960 ± 0.008	0.981 ± 0.012	0.969 ± 0.008	0.969 ± 0.008	0.971 ± 0.007
N_{eff}	2.86 ± 0.19	3.16 ± 0.30	2.95 ± 0.22	2.87 ± 0.21	2.95 ± 0.19
r_{drag}	148.87 ± 1.89	147.06 ± 2.78	148.60 ± 2.25	149.66 ± 2.17	149.17 ± 1.56
Ω_m	0.318 ± 0.009	0.287 ± 0.014	0.305 ± 0.007	0.301 ± 0.007	0.298 ± 0.006
σ_8	0.807 ± 0.010	0.797 ± 0.013	0.795 ± 0.011	0.786 ± 0.010	0.789 ± 0.009
S_8	0.831 ± 0.013	0.779 ± 0.021	0.802 ± 0.013	0.787 ± 0.009	0.787 ± 0.009

DR4 data when combined with WMAP. First, the SPT-3G+WMAP+BAO data mildly suggest a neutrino mass with $\sum m_\nu = 0.22^{+0.056}_{-0.14}$ eV. This constraint is in an excellent agreement with our result based on the Base+BAO data, $\sum m_\nu = 0.2\pm0.107$. This agreement is not surprising given that the PlanckTT-lowℓ data used in our analysis emulates the WMAP measurement, see the related discussion in Sec. 4. The Base + LSS + S$_8$ + SN data significantly improves the accuracy of $\sum m_\nu$ measurement mainly due to the full-shape BOSS likelihood and the weak lensing and photometric galaxy clustering data which have not been considered in Ref. [75]. Second, the ACT-DR4+WMAP+BAO provides a weak upper limit of $\sum m_\nu < 0.19$ eV at 68% CL [75], which is also consistent with our constraint (10).

Performance of the model. The difference in the χ^2 values between the best-fit ΛCDM$+\sum m_\nu$ and ΛCDM models to different datasets is given in Tab. 5.

As the $\Delta\chi^2_{\min}$ is expected to follow the χ^2 distribution with one degree of freedom (the number of extra parameters introduced by ΛCDM$+\sum m_\nu$), we compute the associated confidence interval at which the

ΛCDM$+\sum m_\nu$ model is preferred over ΛCDM. For the Base data analysis we found an insignificant (1.1σ) improvement in the ΛCDM$+\sum m_\nu$ fit over ΛCDM. The Base + LSS + S$_8$ + SN data shows a 2.4σ preference for the ΛCDM$+\sum m_\nu$ scenario. The improvement in the ΛCDM$+\sum m_\nu$ fit over ΛCDM is mainly driven by the LSS data: $\Delta\chi^2_{\text{LSS}} = -4.36/-3.51/-2.61$ for the Base + LSS/Base + LSS + S$_8$/Base + LSS + S$_8$ + SN analyses. This effect can be attributed to a systematically lower value of σ_8 inferred from the BOSS DR12 data [12,37]. Massive neutrinos suppress the growth of linear density field on scales smaller than neutrino free-streaming length that moves the inferred cosmological constraints into better agreement with the BOSS measurements.

Figure 6 shows the 2d posterior distributions for chosen analyses.

To further assess the robustness of the overall preference for the ΛCDM$+\sum m_\nu$ scenario over ΛCDM, we use the Akaike Information Criteria (AIC) [76] defined by AIC $= \chi^2_{\min} + 2N_p$, where N_p is the number of free parameters in the model. Then, the difference ΔAIC $= \Delta\chi^2_{\min} + 2\Delta N_p$ sets a penalty proportional to
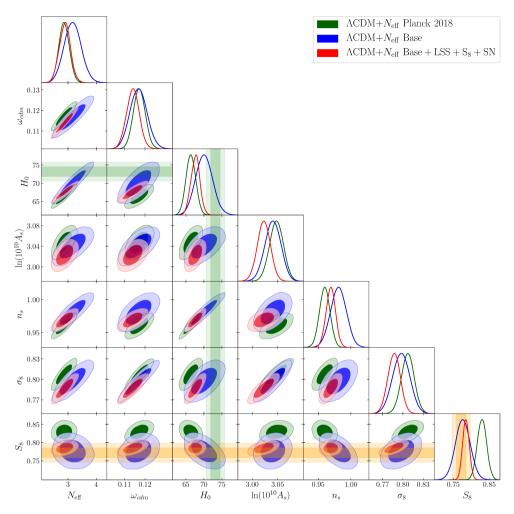
Fig. 7. Marginalized 2d posterior distributions of the cosmological parameters in the ΛCDM+N_{eff} model for Planck 2018 (green), Base (blue) and Base + LSS + S_8 + SN (red) datasets. The Gaussian prior on τ (1) is set. The yellow bands represent 1σ and 2σ constraints on S_8 (2) coming from the photometric surveys (DES-Y3, KiDS, HSC), whereas the green bands refer to the H_0 (4) measurement reported by the SH0ES collaboration

the number of extra parameters introduced by a more complex model ($\Delta N_p = 1$ for ΛCDM+$\sum m_\nu$). The Base data shows a preference in favor of the standard ΛCDM model. In contrast, for the Base+LSS+S_8+SN analysis we found ΔAIC $= -3.91$, which corresponds to a positive preference for the ΛCDM+$\sum m_\nu$ scenario over ΛCDM. Our result is stable against removing S_8 or SN datasets. This reinforces the notion that the LSS data plays a crucial role in constraining the neutrino mass.

6.2. ΛCDM+N_{eff}

We proceed with the ΛCDM+N_{eff} scenario. Table 7 presents the 1d marginalized constraints on cosmological parameters in the ΛCDM+N_{eff} model.

Let us highlight the key differences between our approach and the full Planck analysis. As previously, the Base data suggests a significantly lower S_8 compared to the Planck 2018 analysis, pulling the S_8 value into consistency with the low-redshift probes (2) For the effective number of relativistic degrees of freedom we found $N_{\mathrm{eff}} = 3.16 \pm 0.30$. While our estimate agrees with the Planck 2018 result [3], it allows for considerably larger values of N_{eff}, leading to a moderately higher H_0.

It is interesting to compare our constraint with the result of the full Planck data analysis after marginalizing over the lensing information contained in the CMB power spectra. Allowing arbitrary gravitational lensing in the Planck TT,TE,EE maps one gets $H_0 = 68.2 \pm 1.6\,\mathrm{km\cdot s^{-1}\cdot Mpc^{-1}}$ [15]. This estimate agrees well with both the Base and Planck 2018 data

Table 7. The $\Delta\chi^2_{\min}$ and ΔAIC values between the best-fit ΛCDM+$N_{\rm eff}$ and ΛCDM models to different datasets

Parameter	Base	Base+LSS	Base+LSS +S$_8$	Base+LSS +S$_8$+SN
$\Delta\chi^2_{\min}$	-1.45	$+0.1$	-1.26	-1.68
ΔAIC	$+0.55$	$+2.1$	$+0.74$	$+0.32$

Table 8. Parameter estimates (mean value with 1σ error bars and best fit value in the parentheses) in the phantom-crossing dark energy model. The upper limits are given at 95% CL

Parameter	Phantom-crossing Dark Energy (PDE)			
	Base+LSS	Base+LSS +S$_8$	Base+LSS +S$_8$+SH0ES	Base+LSS +S$_8$+SN
a_m	$0.774(0.757)^{+0.037}_{-0.020}$	$0.774(0.772)^{+0.038}_{-0.020}$	$0.735(0.778)^{+0.044}_{-0.036}$	$0.839(0.822)^{+0.048}_{-0.049}$
α	$8.1(6.6)^{+2.6}_{-3.7}$	$8.0(7.6)^{+2.5}_{-3.6}$	$4.7(6.3)^{+1.1}_{-1.6}$	$1.8(1.3)^{+0.6}_{-1.2}$
β	$14.2(11.0)^{+6.7}_{-8.7}$	$14.1(11.7)^{+6.8}_{-8.4}$	$6.2(11.2)^{+2.2}_{-5.4}$	$< 2.3(0.0)$
$100\,\omega_b$	2.246 ± 0.019	2.245 ± 0.018	2.247 ± 0.018	2.252 ± 0.018
$10\,\omega_{cdm}$	1.165 ± 0.015	1.166 ± 0.011	1.164 ± 0.010	1.157 ± 0.010
H_0	$75.70(75.52)^{+2.05}_{-2.32}$	$75.60(75.36)^{+1.93}_{-2.12}$	$74.26(74.97)^{+1.11}_{-1.12}$	$68.61(68.24)^{+0.78}_{-0.78}$
τ	0.057 ± 0.005	0.057 ± 0.005	0.057 ± 0.005	0.056 ± 0.005
$\ln(10^{10}A_s)$	3.038 ± 0.012	3.038 ± 0.011	3.037 ± 0.011	3.033 ± 0.011
n_s	0.974 ± 0.006	0.974 ± 0.005	0.974 ± 0.005	0.977 ± 0.005
$r_{\rm drag}$	147.93 ± 0.38	147.91 ± 0.31	147.93 ± 0.31	148.08 ± 0.30
Ω_m	0.244 ± 0.015	0.245 ± 0.013	0.253 ± 0.008	0.295 ± 0.007
σ_8	0.854 ± 0.022	0.855 ± 0.021	0.842 ± 0.014	0.791 ± 0.011
S_8	0.770 ± 0.017	0.771 ± 0.010	0.773 ± 0.010	0.784 ± 0.010

analyses. Unlike the $\sum m_\nu$ limit, the error bar on H_0 only moderately increases compared to that in the Planck 2018 analysis. This effect can be attributed to the fact that the H_0 constraint is mainly determined from the position of the first acoustic peak which is barely affected by the CMB gravitational lensing.

Next, we explore the cosmological constraints inferred from the Base + LSS data. Adding the LSS information significantly improves the cosmological measurements. It also provides a 1σ lower value of H_0 being consistent with the Planck 2018 constraint. Adding the S_8 data significantly improves only the accuracy of S_8 measurement, while the other parameter constraints remain largely unchanged.

Finally we consider the supernova measurements. Adding the SN data shrinks the error bars on H_0 and $r_{\rm drag}$ parameters, as the supernova sample fixes the background cosmology at low redshifts which helps to lift the degeneracies between $N_{\rm eff}$ and the ΛCDM cosmological parameters. The Base + LSS + S$_8$ + SN data yields

$$N_{\rm eff} = 2.95 \pm 0.19 \,. \tag{11}$$

This measurement is consistent with the Planck 2018 result. We conclude that the enhanced smoothing of acoustic peaks in the Planck data does not affect the $N_{\rm eff}$ constraint. Our results are in good agreement with the Planck data analysis based on the «unlensed» CMB power spectra [15]. We also found a 1σ higher mean value of the Hubble parameter, $H_0 = 68.02^{+0.94}_{-1.08}\,{\rm km\cdot s^{-1}\cdot Mpc^{-1}}$, which moderately alleviates the Hubble tension down to the 3.2σ level, cf. with (4).

Performance of the model. The $\Delta\chi^2_{\min}$ and ΔAIC values between the best-fit ΛCDM+$N_{\rm eff}$ and ΛCDM estimates for different likelihoods are listed in Tab. 6.2.

In most scenarios, the ΛCDM+$N_{\rm eff}$ model yields a slightly better fit to the data than ΛCDM. According to the AIC, the ΛCDM model is always preferred against ΛCDM+$N_{\rm eff}$.

7. PHANTOM-CROSSING DARK ENERGY

7.1. Model description

We assume that the dark energy equation of state crosses the phantom divide, $w_{\rm DE} = -1$, during the course of its evolution. According to the energy conservation equation for the dark energy fluid, $\frac{d\rho_{\rm DE}}{dt} = -3a^{-1}(1 + w_{\rm DE})\rho_{\rm DE}$, the dark energy density should pass through an extremum at some point in time where $\frac{d\rho_{\rm DE}}{dt}$ changes its sign. Following [34], we expand the dark energy density around its extremum with the time of crossing in terms of scale factor $a = a_m$,

$$\rho_{\rm DE}(a) = \rho_0[1 + \alpha(a - a_m)^2 + \beta(a - a_m)^3], \quad (12)$$

where ρ_0 normalizes the dark energy density, a_m defines the moment when the dark energy density passes through the extremum and α, β describe the course of phantom crossing. Here we choose the present scale factor to be $a_0 = 1$. We also restrict ourselves to the third order in the Taylor expansion because higher order terms cannot be tightly constrained with the present data [34].

Inserting (12) into the Friedman equation for the flat space

$$H^2 = \frac{8\pi G}{3}[\rho_m + \rho_{rad} + \rho_{\rm DE}], \quad (13)$$

we get the following evolution for the Hubble parameter,

$$\frac{H^2(a)}{H_0^2} = \frac{\Omega_m}{a^3} + \frac{\Omega_{rad}}{a^4} +$$
$$+ (1 - \Omega_m - \Omega_{rad})\frac{1 + \alpha(a - a_m)^2 + \beta(a - a_m)^3}{1 + \alpha(1 - a_m)^2 + \beta(1 - a_m)^3}, \quad (14)$$

and for the dark energy equation of state,

$$w_{\rm DE}(a) = -1 - \frac{a[2\alpha(a - a_m) + 3\beta(a - a_m)^2]}{3[1 + \alpha(a - a_m)^2 + \beta(a - a_m)^3]}. \quad (15)$$

At early times ($a \to 0$), the equation of state approaches $w_{\rm DE} = -1$ showing the cosmological constant behavior. It demonstrates that the dark energy equation of state is well defined in the early Universe.

The PDE model is parameterized by (a_m, α, β) as described above. The PDE scenario reduces to the ΛCDM one when $\alpha = \beta = 0$. Note that the parameterization (12) allows for a negative dark energy density $\rho_{\rm DE}$ that introduces greater flexibility to fit the data (see, e. g., [29, 30, 66, 77, 78]).

We implement the background evolution of the PDE through (14) and (15) while assuming no extra sources of clustering except for matter. We vary 9 cosmological parameters: the three PDE (α, β, a_m) and the six standard ΛCDM ($\omega_{cdm}, \omega_b, H_0, \ln(10^{10}A_s), n_s, \tau$). We impose the same flat uniform priors on PDE parameters as in Ref. [34],

$$a_m \in [0, 1], \qquad \alpha \in [0, 30], \qquad \beta \in [0, 30]. \quad (16)$$

7.2. Parameter constraints

Table 8 presents the 1d marginalized constraints on cosmological parameters for different dataset combinations in the PDE model.

Figure 8 shows the final 2d posterior distributions.

We do not show the Base parameter constraints because the CMB data alone cannot break degeneracies present in the PDE model and the dark energy parameters become largely unconstrained [34].

We start with the Base+LSS analysis. For the dark energy parameter we found $a_m = 0.774^{+0.037}_{-0.020}$, $\alpha = 8.1^{+2.6}_{-3.7}$ and $\beta = 14.2^{+6.7}_{-8.7}$. This shows an indication at more than 3σ for phantom crossing in the dark energy sector, considering that that the posterior distributions for α and β are highly non-gaussian. We obtain $H_0 = 75.70^{+2.05}_{-2.32}\,{\rm km\cdot s^{-1}\cdot Mpc^{-1}}$. This constraint is now perfectly consistent within one standard deviation with the SH0ES measurement and deviates from the Planck value [3] by 3.7σ. The increase of the H_0 parameter is due to its positive correlation with α and β as shown in Fig. 8. Importantly, the Base+LSS analysis predicts a substantially lower matter density compared to ΛCDM, namely $\Omega_m = 0.244 \pm 0.015$. This result can be attributed to the phantom period of the dark energy evolution during which $\rho_{\rm DE}$ increases over time resulting in a lower present-day Ω_m [31]. A phantom dark energy also implies a larger growth rate of cosmological matter perturbations [33] that leads to a higher value of σ_8 compared to ΛCDM [11]. *We emphasize that our analysis does not include any priors on late-time parameters but its result is fully consistent with the direct measurements of S_8 (2) and H_0 (4) in the late Universe.*

Next, we proceed with the S_8 data. Adding the S_8 information barely impacts the posterior distributions of the PDE parameters. At the same time, it significantly improves the strength of the S_8 and ω_{cdm} con-

---

[11] It is important here that the dark energy is non-clustering. A clustering phantom dark energy predicts less growth of perturbations than ΛCDM [33].
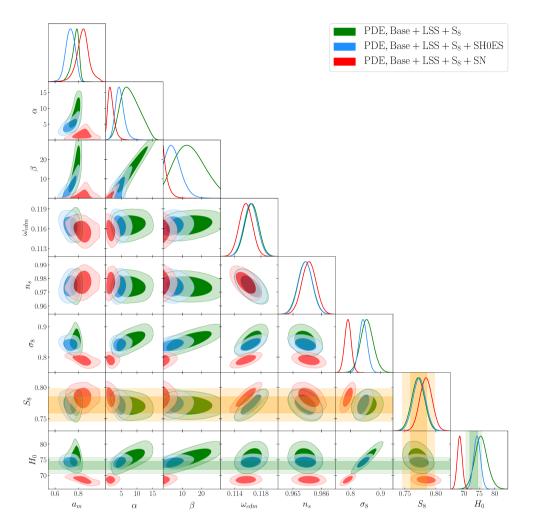
Fig. 8. Marginalized 2d posterior distributions of the cosmological parameters in the PDE model for the $\mathrm{Base} + \mathrm{LSS} + \mathrm{S}_8$ (green), $\mathrm{Base} + \mathrm{LSS} + \mathrm{S}_8 + \mathrm{SH0ES}$ (blue) and $\mathrm{Base} + \mathrm{LSS} + \mathrm{S}_8 + \mathrm{SN}$ (red) datasets. The Gaussian prior on τ (1) is used. The yellow bands represent 1σ and 2σ constraints on S_8, see Eq. (2), it comes from the photometric surveys (DES-Y3, KiDS, HSC), whereas the green bands refer to the Hubble constant H_0 measurement (4) reported by the SH0ES collaboration

straints. Remarkably, the mean value of S_8 remains virtually unchanged, illustrating an excellent agreement between the $\mathrm{Base} + \mathrm{LSS}$ and S_8 datasets.

Since the $\mathrm{Base} + \mathrm{LSS} + \mathrm{S}_8$ and SH0ES data are in agreement now, we can combine them safely together. We apply the entire distance ladder approach which closely reproduces the SH0ES analysis [2] instead of simply imposing a Gaussian constraint on H_0, see Appendix C for a comparison of these approaches. Our joint data analysis demonstrates a decisive evidence for phantom crossing in the dark energy sector, $a_m = 0.735^{+0.044}_{-0.036}$, $\alpha = 4.7^{+1.1}_{-1.6}$ and $\beta = 6.2^{+2.2}_{-5.4}$. As shown in Fig. 8, the SH0ES likelihood breaks the degeneracy between the PDE and standard cosmological parameters that results in significantly tighter con-

straints on the dark energy parameters. We found $H_0 = 74.26^{+1.11}_{-1.12}\,\mathrm{km}\cdot\mathrm{s}^{-1}\cdot\mathrm{Mpc}^{-1}$ which is two times more accurate than the $\mathrm{Base} + \mathrm{LSS} + \mathrm{S}_8$ constraint (without SH0ES). This result can be explained by the positive correlations between α, β and H_0 parameters. The S_8 constraint only barely changes being in an excellent agreement with the low-redshift cosmological probes (2).

We also explore the full Pantheon sample. The supernova absolute magnitude measurement (3) that is used to derive the local H_0 constraint is not compatible with M_B that is necessary to fit CMB, BAO and SN data (see, e. g., [63, 79]). For this reason we combine $\mathrm{Base} + \mathrm{LSS} + \mathrm{S}_8$ and SN data with M_B as a free parameter, but without a SH0ES prior on it. We found

that the Base + LSS + S_8 + SN data reduces the preference for phantom crossing in the dark energy sector leading to $a_m = 0.839^{+0.048}_{-0.049}$, $\alpha = 1.8^{+0.6}_{-1.2}$ and $\beta < 2.3$ (at 95% CL). But it still suggests a mild evidence for a transition in the dark energy density. The matter density parameter is shifted upwards upon adding the SN information, $\Omega_m = 0.295 \pm 0.007$, which is more compatible with the Planck result [3]. Our final constraints on S_8 and H_0 parameters in the PDE scenario are

$$\begin{aligned} S_8 &= 0.784 \pm 0.010, \\ H_0 &= 68.61 \pm 0.78\,\mathrm{km\cdot s^{-1}\cdot Mpc^{-1}}\,. \end{aligned} \quad (17)$$

The S_8 constraint is in good agreement with the low-redshifts probes (2). However, the H_0 value is significantly lower, exhibiting a 3.1σ tension with the SH0ES result (4). This is because the dataset constrains the background evolution in a way which does not allow higher H_0 values. Our result agrees with the previous studies [25, 65–68] which show through the late Universe reconstruction that CMB, BAO and SN data do not allow for a higher expansion rate at low redshifts. This conclusion has been recently reaffirmed in the context of late Universe scenarios with a sudden transition in dark energy sector [63, 79, 80].

7.3. Discussion

In our analysis we combine Base + LSS + S_8 either with the SN catalog or with the SH0ES measurement. The basic reason is that the supernova absolute magnitude that is necessary to fit CMB, BAO and SN data is in a strong disagreement with the local astrophysical calibration via Cepheids. For instance, the Base + LSS + S_8 + SN data predicts the following absolute magnitude of supernova

$$M_B = -19.414 \pm 0.018\,. \quad (18)$$

Our constraint agrees with the results from the standard inverse distance ladder analysis [81, 82] as well as a novel non-parametric approach [83], however it is in a 4.5σ tension with the Cepheid-based measurement (3). This robustly shows that the SN calibration produced by CMB and BAO is not compatible with the SH0ES calibration. Thus, one cannot combine the Base + LSS + S_8 + SN and SH0ES data together until the source of the «supernova absolute magnitude tension» is found (see, e. g., [63, 79]). In what follows, we discuss the potential origins of this tension.

The «supernova absolute magnitude tension» may be caused by astrophysical systematic effects present in the distance ladder measurements. For instance,

average standardized magnitudes of the supernovae in Cepheid hosts and those in the Hubble flow sample may differ due to host-galaxy environmental effects. Recent analyses [84, 85] demonstrate that local age tracers are strongly correlated with the standardized supernova magnitude. Using the classification based on the specific star formation rate, the study of the supernova Factory sample [86] shows that the supernova in predominantly younger environments are fainter than those in predominantly older environments by $\Delta M_B = +0.163 \pm 0.029$. Even when fitting for the specific star formation rate and global stellar mass biases simultaneously, the environment-age offset remains significant at $\Delta M_B = 0.129 \pm 0.032$, for details see [86]. Importantly, the supernova from the Cepheid calibrator sample favors young stellar populations whereas those in the Hubble flow sample do not [85]. It implies that the Cepheid-based calibration (3) may be overestimated by a certain amount that could potentially explain at least part of the «supernova absolute magnitude tension» [86, 87]. The importance of local supernova environmental studies remains highly debated, however (see e. g., Refs. [88, 89]), specifically the impact of such an, astrophysical bias on the H_0 measurements [90, 91].

Another possible source of astrophysical systematics is related to the Cepheid calibration. The Ref. [92] finds a 3σ evidence for a transition in either the color-luminosity relation or the Cepheid absolute magnitude, at a distance in the range between 10 and 20 Mpc. The models where these parameters are fitted by two universal values (one for low galactic distances and one for high galactic distances) are strongly favored over the baseline analysis where no variation is allowed for the Cepheid empirical parameters. A transition in the color-luminosity relation may be attributed to a variation of dust properties in individual galaxies [93, 94], whereas the shift of the Cepheid absolute magnitude could be induced by an abrupt change of fundamental physic [92]. These results have interesting implications in the context of the H_0 measurements. Allowing for the Cepheid color-luminosity relation to vary between galaxies, the H_0 constraints inferred from individual anchors ranges from $H_0 = 68.1 \pm 3.5\,\mathrm{km\cdot s^{-1}\cdot Mpc^{-1}}$ to $H_0 = 76.7 \pm 2.0\,\mathrm{km\cdot s^{-1}\cdot Mpc^{-1}}$ [93]. Next, the Ref. [94] investigates the sensitivity of the H_0 constraint to color excess cuts in the Cepheid data. By removing the reddest Cepheids in order to minimize the impact of dust extinction, they obtain $H_0 = 68.1 \pm 2.6\,\mathrm{km\cdot s^{-1}\cdot Mpc^{-1}}$.

The «supernova absolute magnitude tension» may eventually hint at a possible failure in the standard cosmological scenario and the necessity for new physics.

Since the two measurements, (3) and (18), are performed at different redshift ranges, this mismatch may indicate a transition in the absolute magnitude with amplitude $\Delta M_B \simeq -0.2$ at $z \lesssim 0.01$. Such transition can be achieved by a sudden change of the value of the effective gravitational constant which modifies the supernova intrinsic luminosity, for detail see [95, 96]. Ref. [95] shows that a reduction of the effective gravitational constant at $z > 0.01$ by about 10% would bring the Cepheid-based absolute magnitude of supernova (3) into agreement with the CMB calibration (18). This scenario also addresses the S_8 tension due to the lower value of the gravitational constant at early times. The required amplitude of the M_B transition can be smaller if the transition in gravity sector is accompanied by a rapid change in the dark energy equation of state, for detail see [96].

We conclude that the «supernova absolute magnitude tension» may be affected by astrophysical systematics and/or new physics in gravity sector. The purpose of this paper is not to explore the astrophysical effects or modifications of gravity. Therefore, we adopt an agnostic approach for a possible value of the supernova standardized magnitude. To do so, we analyze the $\text{Base} + \text{LSS} + \text{S}_8 + \text{SN}$ and $\text{Base} + \text{LSS} + \text{S}_8 + \text{SH0ES}$ data separately. We emphasize that the models which modify only the late Universe expansion is not capable of solving this tension [96].

Dark energy equation of state and comparison with previous studies. Figure 9 shows the $w_{\text{DE}}(z)$ evolution for the different best-fit models. The $\text{Base}+\text{LSS}+\text{S}_8+\text{SH0ES}$ analysis suggests a strong preference for a phantom crossing in the dark energy sector. Interestingly, $w_{\text{DE}}(z)$ crosses the phantom divide multiple times. Recall that the $\text{Base} + \text{LSS} + \text{S}_8 + \text{SH0ES}$ dataset predicts a significantly lower value of Ω_m (see Tab. 6.2). Our results thus agree with the model-independent analysis [31] showing that multiple phantom crossings are expected for lower values of Ω_m. In contrast, $\text{Base}+\text{LSS}+\text{S}_8+\text{SN}$ data demonstrates more modest evidence for only one phantom crossing.

Another important aspect of our study relates to the BAO measurements. Table 8 indicates that the PDE constraint on the comoving sound horizon at the end of the baryon drag epoch, r_{drag}, remains essentially the same as in ΛCDM since the PDE scenario does not alter the early-universe evolution. But in this case, one may be concerned that a different late-time Universe evolution may affect the relations $D_A(z)/r_{\text{drag}}$ and $r_{\text{drag}}H(z)$ being precisely measured by the BAO data. Indeed, for monotonic evolution of the dark en-
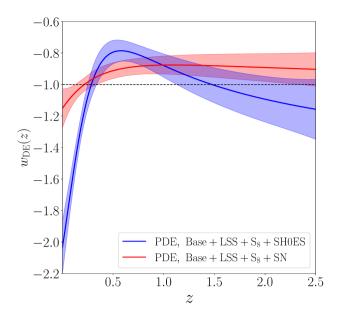

Fig. 9. Behavior of the dark energy equation of state computed for the PDE best-fit models to the $\text{Base} + \text{LSS} + \text{S}_8 + \text{SH0ES}$ (blue) and $\text{Base} + \text{LSS} + \text{S}_8 + \text{SN}$ (red) datasets. The shaded regions represent the 1σ error band. The dashed line corresponds to the cosmological constant behavior $w_{\text{DE}} = -1$

ergy density the radial BAO scale can be translated to the present-day parameter combination $r_{\text{drag}}H_0$ [97], so at constant r_{drag} a shift in H_0 would degrade the fit to the BAO measurements. However, if the behavior of $\rho_{\text{DE}}(z)$ is not-monotonic (akin to PDE), the final result strongly depends on a particular dynamics in the dark energy sector. It suggests that the model with a phantom crossing is capable of fitting the BAO distances regardless of the H_0 value.

To demonstrate the agreement with the BAO measurements, in Fig. 10 we show the evolution of the Hubble parameter and the inverse BAO distance inferred from the different datasets [12].

We found that both PDE analyses are in good agreement with the BAO measurements. Importantly, the $\text{Base} + \text{LSS} + \text{S}_8 + \text{SH0ES}$ model predicts $H_0 \sim 74\,\text{km}\cdot\text{s}^{-1}\cdot\text{Mpc}^{-1}$ while being entirely consistent with the various BAO data. It reinforces that the PDE solution is consistent with the BAO distances calibrated to the CMB-inferred value of r_{drag} [34].

We now compare the dark energy evolution from Fig. 9 to the results of previous analyses. The $w_{\text{DE}}(z)$ behavior derived from the $\text{Base} + \text{LSS} + \text{S}_8 + \text{SH0ES}$

---

[12] The $D_V(z)$ posteriors are always consistent with the constraints inferred from the 6dFGS, MGS and emission line galaxy samples, so these constraints are not shown in the figure
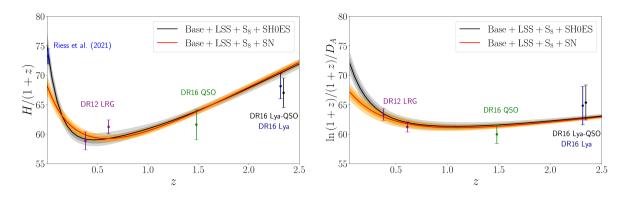
Fig. 10. Behavior of $H(z)/(1+z)$ (left panel) and $\ln(1+z)/(1+z)/D_A$ (right panel) computed for the PDE best-fit models to the Base + LSS + S_8 + SH0ES (black line) and Base + LSS + S_8 + SN (red line) data. The dark and light regions represent the 1σ and 2σ confidence ranges. Both quantities are measured in units of km s^{-1} Mpc^{-1}. The absolute scale for the BAO measurements is set by the best-fit value of the sound horizon optimized to the Base likelihood $r_{\rm drag} = 148.04$ Mpc

Table 9. The $\Delta\chi^2_{\min}$ and ΔAIC values between the best-fit PDE and ΛCDM models to different datasets. We also show the Bayesian factors $\ln B$ calculated for the PDE model with respect to the ΛCDM scenario. Note that the negative value of ΔAIC indicates a preference for the PDE model, while the negative $\ln B$ shows a preference for ΛCDM

Parameter	Base+LSS	Base+LSS +S_8	Base+LSS +S_8+SH0ES	Base+LSS +S_8+SN
$\Delta\chi^2_{\min}$	-12.68	-16.18	-27.39	-3.31
ΔAIC	-4.98	-6.24	-17.92	$+5.27$
$\ln B$	-4.66	-2.65	$+6.90$	-5.48

data agrees well with the model-independent analysis [98] which employs the CMB angular scale, BAO and SH0ES measurements. The multiple phantom crossings are further confirmed by the $H(z)$ reconstruction based on the Pade approximation [31]. In turn, the $w_{\rm DE}(z)$ evolution predicted by the Base+LSS+S_8+SN data is compatible with the non-parametric Bayesian reconstruction of the dark energy evolution [27], which uses CMB, BAO and the uncalibrated supernova sample. This is also broadly consistent with the result of a model-independent $H(z)$ reconstruction [25]. The mild difference can be explained by the SH0ES prior which is used by Ref. [25] but absent in our analysis.

It is also interesting to compare our results with those of the analysis [34] based on the same PDE framework. Using the Planck TTTEEE+lensing CMB data, BAO measurements, uncalibrated supernovae, and the SH0ES prior on H_0, the authors report $H_0 = 70.25 \pm 0.78$ km·s^{-1}·Mpc^{-1}. This H_0 estimate is considerably higher than our Base + LSS + S_8 + SN result, $H_0 = 68.61 \pm 0.78$ km·s^{-1}·Mpc^{-1}. There are two main contributors to this difference. First, the Ref. [34] includes the SH0ES prior on H_0 which shifts

H_0 to higher values. Second, our analysis features the full-shape BOSS measurements and S_8 data which have not been considered in Ref. [34]. We perform the direct comparison of parameter constraints between our analysis and the full Planck approach in Appendix D.

Performance of the model. The $\Delta\chi^2_{\min}$ and ΔAIC values between the best-fit PDE and ΛCDM models to different datasets are given in Tab. 9.

The Base + LSS and Base + LSS + S_8 data show a moderate ($\gtrsim 2.5\sigma$) evidence for the PDE scenario over ΛCDM. This preference is mainly driven by an improvement of the fit to the full-shape BOSS DR12 data: $\Delta\chi^2_{\rm LSS, full-shape} = -15.33$ and -14.07 for Base + LSS and Base + LSS + S_8 data, respectively. Adding the SH0ES measurement raises the evidence for the PDE scenario to the 4.2σ level. In contrast, the PDE model does not significantly improve the fit to Base + LSS + S_8 + SN compared to ΛCDM. According to the AIC, the Base+LSS+S_8+SH0ES data strongly favors the dark energy with phantom crossing, whereas the Base+LSS+S_8+SN combination prefers the ΛCDM model.

Table 10. Parameter estimates (mean value with 1σ error bars and best fit value in the parentheses) in the transitional dark energy model. The upper limits are given at 95% CL

Parameter	Transitional Dark Energy (TDE)			
	Base + LSS	Base + LSS + S_8	Base + LSS + S_8 + SH0ES	Base + LSS + S_8 + SN
w_0	$-1.46(-2.09)^{+0.46}_{-0.32}$	$-1.55(-1.94)^{+0.44}_{-0.32}$	$-1.68(-1.75)^{+0.30}_{-0.26}$	$-1.11(-1.19)^{+0.16}_{-0.07}$
w_1	$-0.79(-1.05)^{+0.30}_{-0.30}$	$-0.78(-1.03)^{+0.30}_{-0.30}$	$-0.68(-1.04)^{+0.26}_{-0.35}$	$-0.72(-0.51)^{+0.25}_{-0.09}$
$z_{\rm tr}$	unconstrained	$< 6.43\,(0.34)$	$< 5.26\,(0.39)$	unconstrained
$\Delta_{\rm tr}$	unconstrained	$< 9.02\,(0.32)$	$< 8.75\,(0.28)$	unconstrained
$100\,\omega_b$	2.242 ± 0.019	2.245 ± 0.019	2.243 ± 0.019	2.249 ± 0.018
$10\,\omega_{cdm}$	1.169 ± 0.015	1.163 ± 0.011	1.171 ± 0.011	1.159 ± 0.010
H_0	$70.46(75.69)^{+1.81}_{-3.10}$	$71.05(74.80)^{+2.30}_{-3.08}$	$72.83(74.36)^{+1.16}_{-1.16}$	$68.17(68.33)^{+0.82}_{-0.74}$
τ	0.057 ± 0.005	0.057 ± 0.006	0.057 ± 0.005	0.056 ± 0.005
$\ln(10^{10}A_s)$	3.038 ± 0.012	3.037 ± 0.011	3.039 ± 0.011	3.035 ± 0.011
n_s	0.974 ± 0.006	0.975 ± 0.005	0.972 ± 0.005	0.976 ± 0.005
$r_{\rm drag}$	147.77 ± 0.37	147.87 ± 0.32	147.80 ± 0.31	148.06 ± 0.30
Ω_m	0.283 ± 0.020	0.277 ± 0.020	0.264 ± 0.009	0.299 ± 0.007
σ_8	0.811 ± 0.027	0.810 ± 0.027	0.826 ± 0.014	0.784 ± 0.011
S_8	0.786 ± 0.018	0.777 ± 0.010	0.775 ± 0.010	0.783 ± 0.010

To reliably calculate the preference for the PDE scenario over ΛCDM we perform a Bayesian evidence analysis. Unlike the AIC, the Bayesian model selection approach penalizes models with a large volume of unconstrained parameter space. This method ought to be preferred in model comparison since it addresses the volume in multi-dimensional parameter space which directly controls the lack of predictivity of more complicated models [99].

We compute the Bayesian evidence with the publicly available cosmological code `MCEvidence` [13] [100], having checked that the multi-dimensional integration is robust against changes of integration limits for all MCMC chains analyzed. We calculate the Bayes factor defined as $\ln B \equiv \ln \mathcal{Z}_{\rm PDE} - \ln \mathcal{Z}_{\Lambda{\rm CDM}}$ where $\mathcal{Z}$ is the Bayesian evidence for a given model, and show the result in Tab. 7.3. A negative (positive) value of the Bayes factor $\ln B$ shows that the ΛCDM (PDE) model is preferred. According to the revised Jeffreys scale by Kass and Raftery [101], we will have for $0 \le |\ln B| < 1$ a weak preference, for $1 \le |\ln B| < 3$ a positive preference, for $3 \le |\ln B| < 5$ a strong preference, and for $|\ln B| \ge 5$ a very strong preference. We found that if the SH0ES dataset is not included the ΛCDM is always the preferred model as the PDE model in-

troduces new parameter degeneracy directions which are poorly constrained by the data. In contrast, the Base + LSS + S_8 + SH0ES combination suggests a very strong preference for the PDE scenario over ΛCDM. This happens because the available parameter space in the PDE sector significantly shrinks upon adding the SH0ES information as shown in Fig. 8.

8. TRANSITIONAL DARK ENERGY

8.1. Model description

We aim to describe a rapid transition in the dark energy sector in a more general way. To that end, we use a model-independent 4-parameter parameterization for the dark energy evolution, suggested in [23],

$$\rho_{\rm DE}(z) = \rho_{\rm DE,0}(1+z)^{3(1+w_{\rm DE}^{\rm eff}(z))}, \tag{19a}$$

$$w_{\rm DE}^{\rm eff} = \frac{1}{2}\left((w_0 + w_1) + (w_1 - w_0)\tanh\frac{z - z_{\rm tr}}{\Delta_{\rm tr}}\rho\right), \tag{19b}$$

where the $w_{\rm DE}^{\rm eff}(z)$ is an effective equation of state (see, e.g., [35]) being related to the physical dark energy

---

[13] https://github.com/yabebalFantaye/MCEvidence

equation of state w_{DE} through

$$w_{\mathrm{DE}}^{\mathrm{eff}}(z) = \frac{1}{\ln(1+z)} \int_0^z w_{\mathrm{DE}}(z') \frac{dz'}{1+z'}. \quad (20)$$

The $w_{\mathrm{DE}}^{\mathrm{eff}}(z)$ reproduces the physical equation of state $w_{\mathrm{DE}}(z)$ only in the regime where $w_{\mathrm{DE}}(z)$ is constant. The w_0 and w_1 are two model parameters which describe the asymptotic behavior of the TDE equation of state in the distant future ($a \to \infty$) and the distant past ($a \to 0$), respectively. The z_{tr} refers to the moment of the transition, whereas the Δ_{tr} parameterizes the steepness of the transition.

In the limit of instantaneous transition ($\Delta_{\mathrm{tr}} \to 0$), the $w_{\mathrm{DE}}^{\mathrm{eff}}$ takes the following form

$$\lim_{\Delta_{\mathrm{tr}} \to 0} w_{\mathrm{DE}}^{\mathrm{eff}}(z) = w_0 + (w_1 - w_0) \times \Theta(z - z_{\mathrm{tr}}), \quad (21)$$

where the Θ denotes the Heaviside function. In this regime, the w_0 and w_1 approach the present and the early values of the physical dark energy equation of state.

The TDE model is fully parameterized by the set of four parameters (w_0, w_1, z_{tr}, Δ_{tr}). Unlike the PDE parameterization, the TDE dark energy density is constrained to be positive. This can bias the results towards smoother evolution of the dark energy density (see, e. g., [29]).

We implement the TDE background evolution through (19) while assuming no perturbations in the dark energy sector. We vary all four TDE parameters (w_0, w_1, z_{tr}, Δ_{tr}) along with the six ΛCDM ones (ω_{cdm}, ω_b, H_0, $\ln(10^{10} A_s)$, n_s, τ). We impose the following uniform priors on TDE parameters:

$$\begin{aligned} w_0 &\in [-\infty, +\infty], & w_1 &\in [-4, 0], \\ z_{\mathrm{tr}} &\in [0, 10], & \Delta_{\mathrm{tr}} &\in [0, 10]. \end{aligned} \quad (22)$$

We assume the wide priors on the z_{tr} and Δ_{tr} parameters. It allows us to obtain meaningful constraints on the TDE transition parameters. We examine the sensitivity of the posterior distributions to the choice of TDE priors in Appendix E.

8.2. Parameter constraints

Table 10 presents the 1d marginalized constraints on cosmological parameters in the TDE model.

Figure 11 shows the resulting 2d posterior distributions.

Here we do not show the results of the Base data analysis because the CMB data alone cannot break the degeneracies present in the TDE sector.

Let us start with the Base + LSS analysis. We find no evidence for a transition in the TDE equation of state, however the posteriors are consistent with this scenario. The posteriors of z_{tr} and Δ_{tr} are prior-dominated, so we do not report the constraints on these parameters. The Base + LSS analysis predicts $H_0 = 70.46^{+1.81}_{-3.10}\,\mathrm{km \cdot s^{-1} \cdot Mpc^{-1}}$. This H_0 estimate is consistent with both the Planck and SH0ES results. We found that the σ_8 constraint is consistent with the ΛCDM expectation but has a four times larger error bar, cf. with Tab. 3. It happens because the TDE scenario introduces extra degrees of freedom that make low-redshift quantities more uncertain relative to the ΛCDM model. The S_8 measurement is entirely consistent with the direct probes (2) in the late Universe.

Next, we include the S_8 data. The data mildly prefers a transition in the TDE equation of state from non-phantom dark energy in the past to phantom dark energy at present. Importantly, our analysis detects upper limits on the TDE transition parameters: $z_{\mathrm{tr}} < 6.43$ and $\Delta_{\mathrm{tr}} < 9.02$ at 95% CL. The H_0 constraint is now consistent within one standard deviation with the direct measurement (4), which allows for combining the Base + LSS + S_8 and SH0ES datasets. The mean value of σ_8 increases compared to the ΛCDM result, cf. with Tab. 3. Indeed, the data favors a phantom dark energy at present which implies a larger growth rate of cosmological matter perturbations compared to ΛCDM, as shown in [33]. It also results in a moderately lower Ω_m.

We further examine the cosmological inference from the Base + LSS + S_8 + SH0ES data. The preference for a transition from quintessence to a phantom dark energy gets stronger when adding the SH0ES information. In particular, the data provides evidence of at least 3σ in favor of $w_0 < -1$. The upper bounds on the TDE transition parameters also strengthen: $z_{\mathrm{tr}} < 5.26$ and $\Delta_{\mathrm{tr}} < 8.75$ at 95% CL. Our analysis yields $H_0 = 72.83 \pm 1.16\,\mathrm{km \cdot s^{-1} \cdot Mpc^{-1}}$, which is in excellent agreement with the SH0ES constraint. Interestingly, the mean value of σ_8 increases compared to the Base + LSS + S_8 (without SH0ES) result. This effect can be attributed to a lower w_0 that further boosts the growth of matter perturbations [33]. Despite this fact, the S_8 constraint is entirely consistent with the direct probes (2) due to a lower value of Ω_m.

Again, the supernova absolute magnitude that is necessary to fit the CMB, BAO and SN data is not compatible with the local astrophysical calibration (3), as discussed in Sec. 7.3. For this reason, we combine the Base + LSS + S_8 and SN data without SH0ES. Our results do not indicate any evidence for a transition in
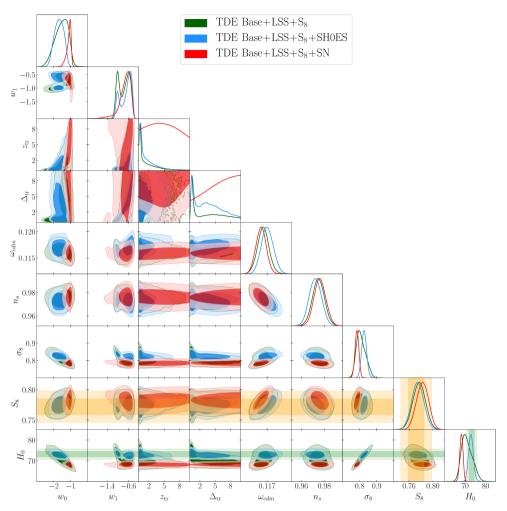
Fig. 11. Marginalized 2d posterior distributions of the cosmological parameters in the TDE model for the Base + LSS + S_8 (green), Base + LSS + S_8 + SH0ES (blue) and Base + LSS + S_8 + SN (red) datasets. The Gaussian prior on τ (1) is always adopted. The yellow bands represent 1σ and 2σ constraints on S_8 (2) coming from the photometric surveys (DES-Y3, KiDS, HSC), whereas the green bands refer to the H_0 measurement (4) reported by the SH0ES collaboration

the TDE equation of state. The z_{tr} and Δ_{tr} parameters become largely unconstrained, and the behavior of dark energy approaches that of the cosmological constant. Therefore, the σ_8 value is now consistent with the ΛCDM result, cf. with Tab. 5.2. As expected, adding the SN data shifts the matter density parameter towards the Planck value: $\Omega_m = 0.299 \pm 0.007$. Our final constraints on S_8 and H_0 in the TDE scenario read

$$S_8 = 0.783 \pm 0.010,$$
$$H_0 = 68.17^{+0.82}_{-0.74}\,\mathrm{km\cdot s^{-1}\cdot Mpc^{-1}}. \tag{23}$$

The S_8 constraint agrees with the direct probes of this parameter in the late Universe (2). On the other hand, the H_0 estimate is in a 3.3σ tension with the SH0ES constraint (4). Our results show the inability of the

TDE model to resolve the Hubble tension, in agreement with the previous studies of late-time Universe modifications (see, e. g., [25, 65–68]).

8.3. Discussion

For the sake of completeness, we present the constraint on the supernova absolute magnitude in the TDE scenario inferred from the Base + LSS + S_8 + SN data,

$$M_B = -19.411 \pm 0.016. \tag{24}$$

This estimate is in perfect agreement with the PDE result (18) and with inverse distance ladder measurements [81–83] while being in a significant, 4.5σ, tension with the local astrophysical calibration via Cepheids (3). This clearly shows that the Base + LSS + S_8 + SN

and SH0ES data are not compatible and, therefore, cannot be combined into one dataset.

Dark energy equation of state and comparison with previous studies. In Fig. 12 we show the $w_{\mathrm{DE}}(z)$ evolution for the different scenarios. The Base + LSS + S_8 + SH0ES data predicts a relatively sharp transition in the dark energy equation of state with $z_{\mathrm{tr}}^{\mathrm{best\text{-}fit}} = 0.39$ and $\Delta_{\mathrm{tr}}^{\mathrm{best\text{-}fit}} = 0.28$. In contrast, the Base+LSS+S_8+SN analysis suggests a very broad transition in the dark energy sector, consistent with the cosmological constant.

To demonstrate the agreement of TDE results with the BAO measurements, in Fig. 13 we show the behavior of the Hubble parameter and the inverse BAO distance inferred from the different datasets. The Base+LSS+S_8+SH0ES analysis agrees with the BAO distances while providing a higher value of H_0 consistent with SH0ES. The Base + LSS + S_8 + SN estimate is also consistent with the BAO data but delivers a smaller H_0, achieving better agreement with the Planck result.

It is important to compare our results with the previous analysis [23] based on the same TDE parameterization. Basically, the CMB, BAO, and SN data and a SH0ES-like 1% prior on H_0 in combination prefer a rapid transition in the dark energy equation of state from $w_{\mathrm{DE}} > -1$ at present to val-
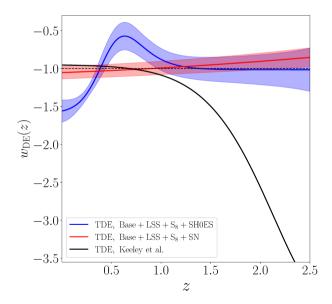
ues much less than -1 by $z \simeq 2$. In Fig. 12 we show the median result of the Gaussian Process inference fitted in the TDE framework ($w_0 = -0.95$, $w_1 = -1.95$, $z_{\mathrm{tr}} = 2.5$, $\Delta_{\mathrm{tr}} = 0.9$) [23]. In contrast, our Base + LSS + S_8 + SH0ES analysis demonstrates a sharper transition from a phantom dark energy at present to nearly the cosmological constant at $z > 1$. The difference in the $w_{\mathrm{DE}}(z)$ behavior can be attributed to the fact that the Ref. [23] utilizes the SH0ES-like prior on H_0 together with uncalibrated SN data, a combination that is not compatible with CMB+BAO (see, e. g., [25, 65–68]). Accordingly, the TDE analysis [23] favors $w_{\mathrm{DE}} > -1$ at present, leading to a slower growth of perturbations, whereas our analysis predicts $w_{\mathrm{DE}} < -1$ today and therefore an enhanced growth of cosmic structures [33].

A recent study [26] presented a model-independent analysis of evolving dark energy with massive neutrinos. Specifically, the authors used a four parameter model for the physical dark energy equation of state $w_{\mathrm{DE}}(z)$ which is different from our parameterization of $w_{\mathrm{DE}}^{\mathrm{eff}}(z)$. This analysis also features a neutrino mass as a free parameter whereas we assume $\sum m_\nu = 0.06\,\mathrm{eV}$. When all data are put together, the authors reported the $w_{\mathrm{DE}}(z)$ evolution to be broadly consistent with the cosmological constant. This generally agrees with our results based on the Base + LSS + S_8 + SN data, see Fig. 12, although we cannot directly compare the parameter constraints given the differences in our approaches.

Performance of the model. Table 11 presents the $\Delta\chi_{\mathrm{min}}^2$ and ΔAIC values calculated for the best-fit TDE and ΛCDM models to different datasets.

The Base + LSS + S_8 + SH0ES data provides a 3.8σ evidence for the TDE model. This effect is attributed to the higher value of H_0 in the TDE scenario which significantly improves the fit to the SH0ES data, namely $\Delta\chi_{\mathrm{SH0ES}}^2 = -12.47$. In turn, the Base + LSS + S_8 + SN data shows a marginal evidence for the TDE scenario over ΛCDM. According to the AIC, the Base + LSS + S_8 + SH0ES data strongly favors the TDE scenario against ΛCDM, whereas the Base + LSS + S_8 + SN combination prefers the base-ΛCDM model.

We also compute the Bayes factor $\ln B$ for different datasets and show the results in Tab. 8.3. The Base+LSS+S_8+SH0ES data shows only a weak preference for the TDE model over ΛCDM. This result can be explained by the largely unconstrained parameter space in the TDE sector that harshly penalized this model (see Fig. 11).
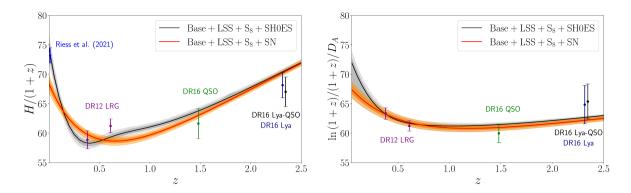

Fig. 12. Behavior of the dark energy regular equation of state for the TDE best-fit models to Base+LSS+S_8+SH0ES (blue) and Base+LSS+S_8+SN (red) datasets, as well as the result of the Gaussian Process inference from [23] (solid black). The dashed line corresponds to $w_{\mathrm{DE}} = -1$. The shaded regions represent the 1σ error band

Fig. 13. Behavior of $H(z)/(1+z)$ and $\ln(1+z)/(1+z)/D_A$ in the TDE model. The dark and light regions display the 1σ and 2σ confidence ranges. Both quantities are measured in units of $\mathrm{km\,s^{-1}\,Mpc^{-1}}$. The absolute scale for the BAO measurements is set by the best-fit value of the sound horizon optimized to the Base likelihood $r_{\mathrm{drag}} = 148.04\,\mathrm{Mpc}$

Table 11. The $\Delta\chi^2_{\min}$ and ΔAIC values between the best-fit TDE and ΛCDM models to different datasets. We also show the Bayesian factors $\ln B$ calculated for the TDE model with respect to the ΛCDM scenario. Note that the negative value of ΔAIC indicates a preference for the TDE scenario, while the negative $\ln B$ shows a preference for ΛCDM

Parameter	Base+LSS	Base+LSS +S_8	Base+LSS +S_8+SH0ES	Base+LSS +S_8+SN
$\Delta\chi^2_{\min}$	-10.68	-11.42	-28.99	-2.83
ΔAIC	-2.94	-4.99	-14.68	$+7.39$
$\ln B$	-13.91	-7.48	$+1.19$	-6.51

9. CONCLUSIONS

In this work, we have presented new constraints on cosmological parameters in ΛCDM and several of its extensions, using a multi-source dataset that includes CMB measurements, large-scale structure, and supernovae data. As the primary CMB observations we consider the SPT-3G polarization, SPTpol gravitational lensing, and Planck temperature measurements.

Our analysis yields systematically lower values of S_8, with $S_8 = 0.790 \pm 0.009$ being entirely consistent with low-redshift cosmological probes, resolving the so-called S_8 tension present at the 3.3σ significance level between weak lensing and photometric galaxy clustering data and the baseline Planck CMB spectra. This suggests that the tension was at least partly driven by the excess smoothing of the Planck TT power spectrum peaks and troughs that increases the late-time amplitude.

We have then explored two simple extension of ΛCDM. In the ΛCDM+$\sum m_\nu$ model, the Base + LSS + S_8 + SN data combination exhibits a 4.1σ preference for a non-zero sum of neutrino masses, $\sum m_\nu = 0.221 \pm 0.055\,\mathrm{eV}$. In the full Planck analysis, a lensing-like anomaly and the standard

BAO+RSS treatment of LSS data strengthen the constraints on neutrino masses, making such high values of $\sum m_\nu$ seem implausible [3]. We conclude that, in light of the ongoing cosmological tensions, future CMB and LSS data, such as The Simons Observatory [102] and CMB-S4 experiments [103], must be carefully considered before definitively excluding the region $\sum m_\nu \gtrsim 0.2\,\mathrm{eV}$. Additionally, we have revisited the parameter constraints in the ΛCDM+N_{eff} scenario, with our constraint on N_{eff} being consistent with the Planck baseline analysis.

Finally, we have investigated the possibility of dynamical dark energy with a late-time phantom transition through two phenomenological approaches, reconstructing either the dark energy density (PDE) or the effective dark energy equation of state (TDE). Here, our findings emphasize the importance of properly reconciling the early- and late-Universe observations when attempting to resolve the Hubble tension. On the surface, explicitly fixing the absolute magnitude M_B to the value obtained from the local distance ladder calibration does seem to favor the dynamical dark energy models and produce H_0 values consistent with local measurements. However, it merely transfers the ten-
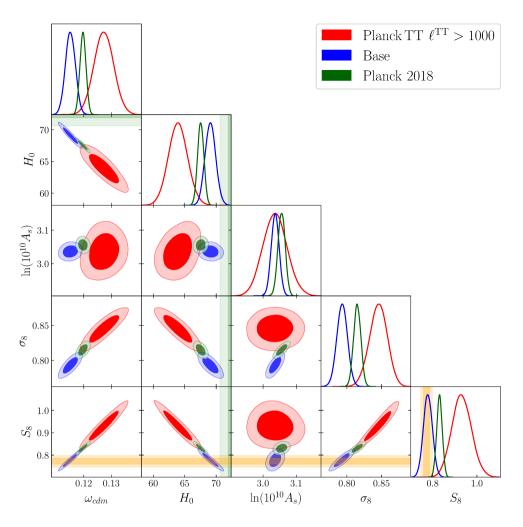
Fig. 14. 2d posterior distributions of the cosmological parameters inferred for the Planck TT $\ell^{\mathrm{TT}} > 1000$ (red), Base (blue) and Planck 2018 (green) datasets. The Gaussian prior on τ (1) is adopted

sion from H_0 to M_B, as letting M_B be freely calibrated by CMB and LSS data shifts it by 4.5σ and in both models restricts H_0 to $\simeq 68\,\mathrm{km\cdot s^{-1}\cdot Mpc^{-1}}$, strongly favoring ΛCDM. This implicit tension was often overlooked by analyses utilizing simple H_0 or M_B priors in conjunction with the full Pantheon catalog and CMB data. This result can be generalized to most late-time modifications of ΛCDM, rendering them unsuitable as solutions to the Hubble crisis.

Overall, the combination of SPT-3G and Planck CMB measurements with the full-shape treatment of LSS data has proven to be a robust baseline for testing the consistency of models typically evaluated using the full Planck dataset and BAO information.

Our work can be continued in multiple ways. A natural extension of our analysis would be to include the recent SPT-3G measurements of TT power spec-

trum [104]. In addition, it would be interesting to consider the alternative ACT-DR4 CMB measurements at small angular scales [17]. Finally, our analysis can be improved by including the full-shape analysis of the eBOSS quasar sample [105, 106] and the galaxy bispectrum multipoles [107] which can potentially yield a significant information gain in extended cosmological scenarios. We leave these tasks to future work.

ical calculations have been performed with the Hy-briLIT heterogeneous computing platform (LIT, JINR) (http://hlit.jinr.ruhttp://hlit.jinr.ru) and the Helios cluster at the Institute for Advanced Study, Princeton.

A. CHOICE OF MULTIPOLE CUTOFF

Here, we quantify the consistency between the Base dataset and the Planck TT $\ell^{\mathrm{TT}} > 1000$ spectrum [14]. We also assess the impact of adding the Planck TT high-ℓ data gradually to the Base dataset combination.

First, we explore the consistency between the Base and Planck TT $\ell^{\mathrm{TT}} > 1000$ data at the level of posterior distributions. Figure 14 shows the two-dimensional parameter constraints inferred from these datasets together with the Planck 2018 results.

The corresponding 1d marginalized parameter constraints are listed in Tab. 12.

The Base and Planck TT $\ell^{\mathrm{TT}} > 1000$ data lead to substantially different posteriors which 2d projections can deviate at more than 2σ. In particular, the Planck TT high-ℓ measurements predict a 3.4σ higher value of σ_8 compared to the Base data analysis. Combined with a moderately higher Ω_m, it results in $S_8 = 0.933 \pm 0.044$, which exhibits a 3.5σ tension with the low-redshift cosmological probes (2). The Planck TT $\ell^{\mathrm{TT}} > 1000$ data also predicts a considerably lower value of the Hubble parameter, $H_0 = 63.93 \pm 1.56\,\mathrm{km \cdot s^{-1} \cdot Mpc^{-1}}$, which is in a 4.6σ tension with the SH0ES measurement. It also deviates from the Planck 2018 result by 2.2σ.

Even though the posterior distributions give insight into the parameter discrepancy, it is important to assess the significance of the corresponding tension in the full ΛCDM parameter space. To quantify the overall consistency between disjoint datasets we consider the metric [15]

$$\chi^2 = (\mathbf{p}_1 - \mathbf{p}_2)^{\mathrm{T}}(C_1 + C_2)^{-1}(\mathbf{p}_1 - \mathbf{p}_2), \qquad (25)$$

where $\mathbf{p}_i$ is the vector of parameter means and C_i is the posterior covariance, both for a given experiment i. We carry out the comparison in the 5-parameter space $(\omega_{cdm}, \omega_b, H_0, n_s, \ln(10^{10}A_s))$. We ignore τ because

---

[14] For clarity, in this section we will refer to multipoles in the TT power spectra as ℓ^{TT} in order to discriminate between temperature and polarization multipole ranges.

[15] The measure (25) gives a reasonable estimate of the parameter discrepancy only in the limit of multivariate Gaussian posterior distribution. As shown in Fig. 14, the parameter posteriors inferred from the Base and Planck TT $\ell^{\mathrm{TT}} > 1000$ datasets are reasonably Gaussian, so the metrics defined below gives a good measure of consistency in the full parameter space.

the τ information went into both sets of estimated parameters through the Gaussian prior (1), though we have explicitly checked that the comparison in the parameter space $(\omega_{cdm}, \omega_b, H_0, n_s, A_s e^{-2\tau})$ gives identical results.

Then, we compute the probability to exceed χ^2 (for a χ^2 distribution with degrees of freedom equal to the number of free parameters) and convert it into the equivalent number of σ using the standard Gaussian interpretation. We also scan for $\max(|\Delta\mathbf{p}/\sigma_p|)$ (σ_p is the posterior error given by the square root of a diagonal element of $C_1 + C_2$) and report the most deviant parameter(s). We cite the corresponding difference in units of σ_p.

Our results are summarized in Tab. 13.

with a comparison of the Base and Planck TT $\ell^{\mathrm{TT}} > 1000$ data given in the first row. We identified a 2.4σ tension between these datasets in the 5-dimensional parameter space. Note that individual cosmological parameters, like ω_{cdm} and H_0, deviate by 3σ. These parameters are of the most interest because they relate to the low-redshift cosmological probes. The H_0 measurement is currently the center of great attention due to the Hubble tension, whereas ω_{cdm} determines the broadband shape of the galaxy power spectrum and controls the growth rate of cosmological matter perturbations. As an additional cross-check, we assess the consistency between the Base combination and Planck TT $\ell^{\mathrm{TT}} > 1000$ data in the parameter space $(\omega_{cdm}, \omega_b, H_0, n_s, \sigma_8)$, where we consider the late-time σ_8 instead of $\ln(10^{10}A_s)$. We found that the significance of the overall tension between the datasets increases by 0.2σ compared to that in Tab. 13.

It is interesting to know if our particular choice of $\ell^{\mathrm{TT}} = 1000$ greatly affected the results. Additionally, we investigate the effect of splitting the Planck TT spectrum at $\ell^{\mathrm{TT}} = 800$. This choice roughly corresponds to an even division of the Planck TT constraining power on ΛCDM parameters coming from the $\ell^{\mathrm{TT}} < 800$ and $\ell^{\mathrm{TT}} > 800$ multipole ranges which has been extensively discussed in [14]. Specifically, we perform a comparison of the SPT-3G + Lens + PlanckTT ($\ell^{\mathrm{TT}} < 800$) and Planck TT $\ell^{\mathrm{TT}} > 800$ datasets and show the results in the second row of Tab. A. We found that our findings are stable against the choice of the multipole cutoff scale in the TT power spectrum.

Reference [14] claims that the power deficit in the Planck TT spectrum at $\ell \lesssim 30$ plays an important role in driving disagreement between the Planck low- and high-multipole parameter constraints. It is thus interesting to explore the effect of the entire $\ell^{\mathrm{TT}} < 30$ region on our results. To that end, we quantify the

Table 12. Parameter constraints for different datasets with 1σ errors in the ΛCDM model

Parameter	ΛCDM		
	Planck 2018	Base	Planck TT $\ell^{\mathrm{TT}} > 1000$
$100\,\omega_b$	2.241 ± 0.015	2.255 ± 0.020	2.115 ± 0.094
$10\,\omega_{cdm}$	1.197 ± 0.011	1.151 ± 0.018	1.273 ± 0.037
H_0	67.53 ± 0.50	69.09 ± 0.84	63.93 ± 1.56
τ	0.060 ± 0.005	0.058 ± 0.005	0.058 ± 0.005
$\ln(10^{10} A_s)$	3.055 ± 0.011	3.036 ± 0.012	3.036 ± 0.037
n_s	0.967 ± 0.004	0.977 ± 0.006	1.000 ± 0.048
Ω_m	0.313 ± 0.007	0.290 ± 0.010	0.366 ± 0.025
σ_8	0.815 ± 0.005	0.793 ± 0.008	0.845 ± 0.013
S_8	0.833 ± 0.013	0.780 ± 0.020	0.933 ± 0.044

Table 13. Consistency of different datasets (first and second columns) as determined from the metric (25) (third column) and the shift in the most deviant parameter(s) (fourth column)

dataset 1: SPT-3G+Lens+Planck TT	dataset 2: Planck TT	Test	
		χ^2	max-param
$\ell^{\mathrm{TT}} < 1000$ (Base)	$\ell^{\mathrm{TT}} > 1000$	2.4σ	3.0σ (ω_{cdm}, H_0)
$\ell^{\mathrm{TT}} < 800$	$\ell^{\mathrm{TT}} > 800$	2.3σ	3.1σ (ω_{cdm})
$30 < \ell^{\mathrm{TT}} < 1000$	$\ell^{\mathrm{TT}} > 1000$	2.3σ	2.8σ (ω_{cdm}, H_0)
$30 < \ell^{\mathrm{TT}} < 800$	$\ell^{\mathrm{TT}} > 800$	2.1σ	2.9σ (ω_{cdm})

consistency between the different datasets while excising the range $\ell^{\mathrm{TT}} < 30$ and show the outputs in the third and fourth rows of Tab. A. Our results remain largely unchanged. Thus, the large-scale temperature dip does not contribute to the tension between the Base and Planck TT $\ell^{\mathrm{TT}} > 1000$ data.

We also investigate the effect of fixing the foreground parameters of the Planck data to the best-fit values inferred from the entire Planck TT spectrum rather than allowing them to vary separately in the $\ell^{\mathrm{TT}} < 1000$ and $\ell^{\mathrm{TT}} > 1000$ fits (while still varying all foreground parameters of the SPT-3G data). We found that the tension between the Base and Planck TT $\ell^{\mathrm{TT}} > 1000$ data persists at the 2.4σ level while individual cosmological parameters differ by up to 2.9σ. Overall, the choice of Planck foreground parameters does not impact our conclusion. It agrees with previous studies [14,71] showing that the results are not very sensitive to the specific assumptions about foreground modeling.

Let us now explore the sensitivity of our CMB-based parameter constraints to the choice of a Planck TT data cutoff. To that end, we perform an analysis of the SPT-3G + SPTlens + Planck TT data with the Planck TT spectrum taken at $\ell^{\mathrm{TT}} < \ell^{\mathrm{TT}}_{\mathrm{max}}$. In Fig. 15 we show the resulting parameter constraints for the following multipole cuts $\ell^{\mathrm{TT}}_{\mathrm{max}} = 800, 1000, 1500, 2000$ and 2500 (up to the nearest bin). Note that the choice $\ell^{\mathrm{TT}}_{\mathrm{max}} = 1000$ corresponds to the Base combination whereas the $\ell^{\mathrm{TT}}_{\mathrm{max}} = 2500$ refers to the entire Planck TT spectrum.

We found that the parameter measurements are stable across $\ell^{\mathrm{TT}}_{\mathrm{max}} \in [600, 1000]$. Interestingly, the combined data approach leads to significantly tighter constraints on all cosmological parameters when compared with the Planck TT $\ell < 800$ analysis from Ref. [14] (shown by yellow diamonds) [16]. This effect can be attributed to the SPT polarization and gravitational lensing measurements which sharpen the parameter constraints by a factor of 2. For $\ell^{\mathrm{TT}}_{\mathrm{max}} > 1000$ the means of cosmological parameters drift away from the values found in our baseline analysis (labeled as Base). As far as the entire Planck TT data is included, we found $\leq 1.7\sigma$ shifts in the parameter posteriors from the Base

---

[16] Note that the mean of A_s reported in [14] is systematically higher due to the larger value of optical depth, $\tau = 0.07 \pm 0.02$, adopted in this analysis. For clarity, we decided to show the original results from [14].
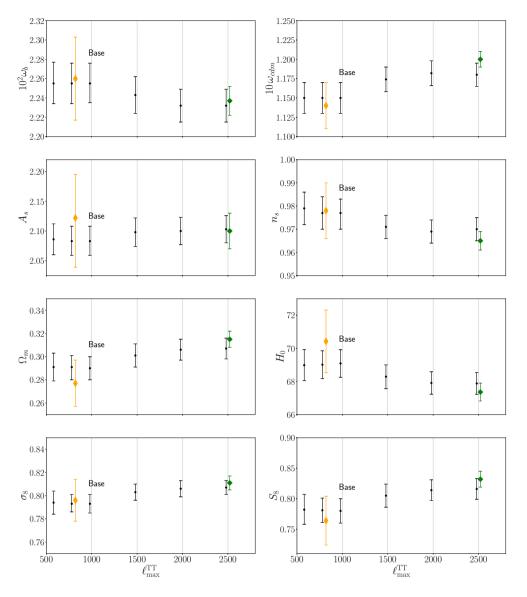
Fig. 15. Marginalized parameter estimates (1σ error bars) inferred from the SPT-3G+SPTlens+Planck TT data with the Planck TT spectrum analyzed up to a certain cutoff point $\ell^{\mathrm{TT}} < \ell^{\mathrm{TT}}_{\max}$. We also display the results of the official Planck TT $\ell^{\mathrm{TT}} < 800$ analysis [14] (yellow diamonds) as well as the Planck legacy release constraints [3] (green diamonds)

results. This difference originates from the Planck high-ℓ TT spectrum which, as we showed before, is in a 2.4σ tension with the Base data combination. Although the deviation is not very significant, we choose not to combine the Base and the Planck TT $\ell^{\mathrm{TT}} > 1000$ measurements into one dataset.

To summarize this section, our CMB-based results are not sensitive to the choice of the Planck TT cutoff $\ell^{\mathrm{TT}}_{\max} \lesssim 1000$. Our baseline choice $\ell^{\mathrm{TT}}_{\max} = 1000$ roughly corresponds to the maximum multipole accessible to WMAP [72]. Thus, the PlanckTT-lowℓ likelihood can be seen as a proxy for WMAP.

B. PARAMETER DIFFERENCES BETWEEN ANALYSES EMPLOYING SHARED DATA

For the sake of simplicity we consider a one-parameter toy model. The joint log-likelihood in the Gaussian approximation reads

$$\ln L = -\frac{1}{2(1-\rho^2)} \times$$
$$\times \left[\frac{(s-s_1)^2}{\sigma_1^2} - 2\rho\frac{(s-s_1)(s-s_2)}{\sigma_1\sigma_2} + \frac{(s-s_2)^2}{\sigma_2^2} \right],$$
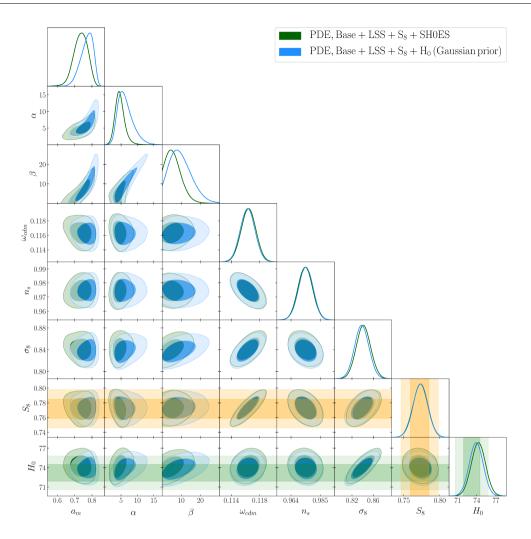(26)

Fig. 16. 2d posterior distributions of the cosmological parameters in the PDE model inferred from the $\mathrm{Base + LSS + S_8 + SH0ES}$ data using the entire distance ladder (green) and the $\mathrm{Base + LSS + S_8 + H_0}$ combination utilizing the Gaussian constraint on H_0 (4) (blue)

where s_i, σ_i denote the means and standard deviations of the parameter s inferred from the individual datasets, and ρ is the correlation between these two measurements. The joint log-likelihood can be cast in a suggestive form,

$$\ln L = -\frac{(s - \bar{s})^2}{2(1 - \rho^2)\sigma_1^2\sigma_2^2(\sigma_1^2 - 2\rho\sigma_1\sigma_2 + \sigma_2^2)^{-1}} - \mathcal{C}\,,$$
(27)

where $\bar{s} = \int L(s)sds / \int L(s)ds$ is the mean value calculated in the joint analysis, and the $\mathcal{C}$ is defined by

$$\mathcal{C} = \frac{(s_1 - s_2)^2}{\sigma_1^2 - 2\rho\sigma_1\sigma_2 + \sigma_2^2}\,.$$
(28)

The term $\mathcal{C}$ defines the tension metric for the posterior s derived from different datasets. The expected standard deviation of the parameter shift is given by

the denominator of (28). For shared datasets, the correlation is positive, $\rho > 0$, so the expected difference in posterior means is always smaller than the posterior error of the two experiments combined in quadrature. Thus, by assessing the parameter difference in terms of the Gaussian error bars of the two datasets, as if they were independent, one underestimates the parameter tension.

C. DISTANCELADDER VS. GAUSSIAN PRIOR ON H_0

In many studies the distance ladder measurements are reduced to a simple Gaussian constraint on H_0. In cosmological scenarios which are phenomenologically close to ΛCDM at late time (including those which only

Table 14. Parameter constraints (mean value with 1σ error bars and best fit value in the parentheses) in the PDE model. The upper limits are given at 95% CL

Parameter	PDE	
	Base+LSS+S_8+SN	Planck 2018+LSS+S_8+SN
a_m	$0.839(0.822)^{+0.048}_{-0.049}$	$0.822(0.817)^{+0.053}_{-0.039}$
α	$1.8(1.3)^{+0.6}_{-1.2}$	$1.7(1.3)^{+0.5}_{-1.3}$
β	$(0.0) < 2.3$	$3.1(2.0)^{+1.0}_{-0.9}$
$100\,\omega_b$	2.252 ± 0.018	2.253 ± 0.012
$10\,\omega_{cdm}$	1.157 ± 0.010	1.181 ± 0.007
H_0	$68.61(68.24) \pm 0.78$	$69.16(68.97) \pm 0.76$
τ	0.056 ± 0.005	0.058 ± 0.005
$\ln(10^{10}A_s)$	3.033 ± 0.011	3.047 ± 0.010
n_s	0.977 ± 0.005	0.971 ± 0.003
r_{drag}	148.08 ± 0.30	147.42 ± 0.21
Ω_m	0.295 ± 0.007	0.295 ± 0.007
σ_8	0.791 ± 0.011	0.815 ± 0.009
S_8	0.784 ± 0.010	0.809 ± 0.008

Table 15. Parameter estimates (mean value with 1σ error bars and best fit value in the parentheses) inferred for the Base + LSS + S_8 + SH0ES data with the baseline priors (22) (Baseline priors) and new priors (29) (New priors). The upper limits are given at 95% CL

Parameter	TDE	
	Baseline priors	New priors
w_0	$-1.68(-1.75)^{+0.30}_{-0.26}$	$-1.67(-1.69)^{+0.42}_{-0.22}$
w_1	$-0.68(-1.04)^{+0.26}_{-0.35}$	$-0.81(-1.07)^{+0.31}_{-0.28}$
z_{tr}	$< 5.26(0.39)$	$< 4.89(0.40)$
Δ_{tr}	$< 8.75(0.28)$	$1.79(0.24)^{+0.20}_{-1.73}$
$100\,\omega_b$	2.243 ± 0.019	2.243 ± 0.019
$10\,\omega_{cdm}$	1.171 ± 0.011	1.168 ± 0.012
H_0	$72.83(74.36) \pm 1.16$	$73.17(74.95)^{+1.30}_{-1.27}$
τ	0.057 ± 0.005	0.057 ± 0.005
$\ln(10^{10}A_s)$	3.039 ± 0.011	3.038 ± 0.012
n_s	0.972 ± 0.005	0.973 ± 0.005
r_{drag}	147.80 ± 0.31	147.87 ± 0.32
Ω_m	0.264 ± 0.009	0.262 ± 0.010
σ_8	0.826 ± 0.014	0.829 ± 0.016
S_8	0.775 ± 0.010	0.774 ± 0.011

modify the early Universe), this approximation is accurate. However, when analyzing models which deviate significantly from ΛCDM at late times using the traditional Gaussian prior on H_0 can bias results and even lead to the spurious detection of new physics [62, 80].

The reason is that the local distance ladder measures distances to supernova in the Hubble flow at $z \gtrsim 0.02$ rather than simply constrain H_0. Thus, the entire distance ladder approach is required for any model which modifies the Universe expansion in this redshift range.
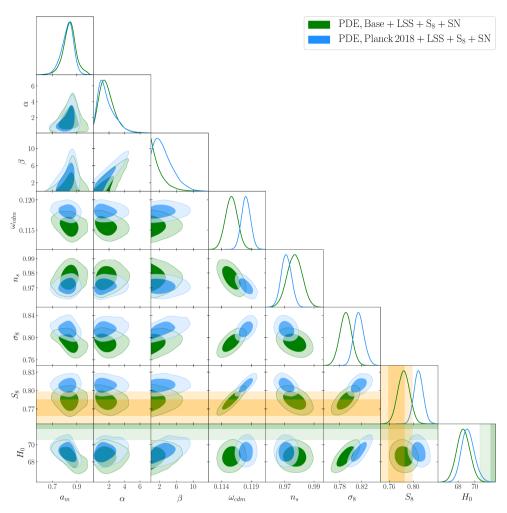
Fig. 17. Marginalized 2d posterior distributions of the cosmological parameters in the PDE model for the $\mathrm{Base + LSS + S_8 + SN}$ (green) and the $\mathrm{Planck\,2018 + LSS + S_8 + SN}$ (red) datasets. The Gaussian prior on τ (1) is set. The yellow bands represent 1σ and 2σ constraints on S_8, see Eq. (2), it comes from the photometric surveys (DES-Y3, KiDS, HSC), whereas the green bands refer to the Hubble constant H_0 measurement (4) reported by the SH0ES collaboration

To showcase the difference in the parameter inference between these two approaches, we explore the parameter constraints in the PDE scenario using the Gaussian constraint on H_0 (4) (dubbed $\mathrm{H_0}$). We analyze the $\mathrm{Base + LSS + S_8 + H_0}$ data and show the resulting posterior distributions of cosmological parameters in Fig. 16.

We found that the results of using the entire distance ladder and the Gaussian prior on H_0 are in good agreement. The actual distance measurements have a modest impact on the distributions of the PDE parameters while the constraints on the ΛCDM cosmological parameters remain virtually intact. This result can be explained by a smooth background evolution in the PDE model (see, e.g., Fig. 9). Note that a sudden low-redshift discontinuity in the Hubble rate breaks down the standard cosmographic expansion of the luminosity distance to supernova that will make the traditional Gaussian constraint on H_0 inadequate [62].

D. PDE ANALYSIS WITH FULL PLANCK LIKELIHOOD

In this Appendix we explore the parameter constraints in the PDE scenario when using the full Planck spectra. We examine the cosmological measurements from the $\mathrm{Planck\,2018 + LSS + S_8 + SN}$ data. The marginalized parameter constraints are listed in Tab. 14.

The corresponding 2d posterior distributions are shown in Fig. 17.

For comparison we also show our baseline results based on the $\mathrm{Base + LSS + S_8 + SN}$ data.
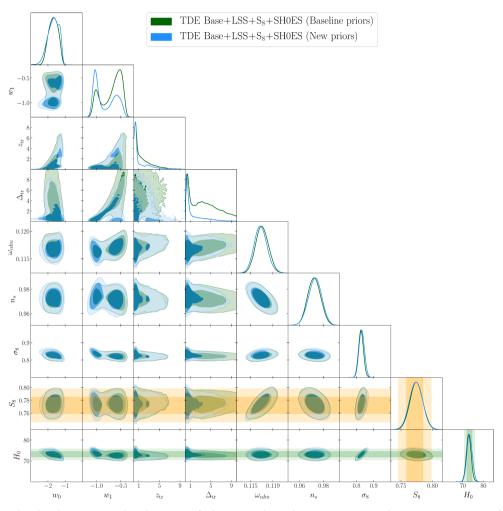
Fig. 18. Marginalized 2d posterior distributions of the cosmological parameters in the TDE scenario inferred from the Base + LSS + S_8 + SH0ES data with the baseline priors (22) (green) and new priors (29) (blue)

The constraints on the dark energy parameters in the two analyses agree, although the Planck 2018 + LSS + S_8 + SN data favors considerably larger values of β. Importantly, the analysis based on the full Planck likelihood predicts a 2.2σ higher value of the late-time fluctuation amplitude, $\sigma_8 = 0.815 \pm 0.009$. This leads to $S_8 = 0.809 \pm 0.008$ which is in a 2.4σ tension with the direct probes (2). This difference can be explained by the enhanced smoothing of acoustic peaks in the Planck spectra which pulls the late-time amplitude to higher values. Our analysis is free from this feature and thus predicts a lower value of S_8 being consistent with the weak lensing and photometric galaxy clustering measurements. Interestingly, the Planck 2018 + LSS + S_8 + SN combination predicts a slightly higher value of the Hubble constant, $H_0 = 69.16 \pm 0.76\,\mathrm{km\cdot s^{-1}\cdot Mpc^{-1}}$. This behavior can be attributed to the observed

degeneracy direction $\sigma_8 h^{-1.2}$ that pulls H_0 to higher values.

In essence, the PDE scenario with the full Planck data slightly alleviates the S_8 tension, whereas the Base + LSS + S_8 + SN results are entirely consistent with the direct measurements (2).

E. PRIOR DEPENDENCE IN TDE MODEL

In the baseline analysis we have followed the previous work [23] and assumed the uniform priors on the TDE parameters z_{tr} and Δ_{tr}. The posterior distributions for these parameters are dominated by the priors, so it raises a concern regarding the prior dependence of TDE results. Here, we examine the sensitivity of parameter constraints to the choice of TDE priors.

Table 16. $\chi^2_{\min}$ values for the best-fit ΛCDM, ΛCDM$+\sum m_\nu$ and ΛCDM$+N_{\text{eff}}$ models to the Base, Base + LSS, Base + LSS + S$_8$ and Base + LSS + S$_8$ + SN datasets

ΛCDM	Base	Base+LSS	Base+LSS+S$_8$	Base+LSS+S$_8$+SN
SPT-3G	519.70	520.01	519.52	519.50
Planck TT, $\ell < 30$	21.09	21.63	21.29	21.29
Planck TT, $30 \leq \ell < 1000$	403.39	403.71	403.71	403.76
Lens	5.55	5.64	5.39	5.39
τ-prior	0.00	0.28	0.72	0.76
LSS, full-shape	–	1070.73	1072.66	1072.57
LSS, BAO	–	7.27	7.62	7.61
S$_8$	–	–	1.85	1.86
SN	–	–	–	1025.63
Total $\chi^2_{\min}$	949.74	2029.25	2032.75	3058.38
ΛCDM$+\sum m_\nu$	Base	Base+LSS	Base+LSS+S$_8$	Base+LSS+S$_8$+SN
SPT-3G	519.43	519.24	519.35	520.75
Planck TT, $\ell < 30$	21.22	21.07	20.96	21.05
Planck TT, $30 \leq \ell < 1000$	403.22	403.57	403.39	404.08
Lens	5.61	5.59	5.76	5.67
τ-prior	0.00	0.02	0.01	0.00
LSS, full-shape	–	1067.93	1068.58	1069.02
LSS, BAO	–	7.26	7.26	7.26
S$_8$	–	–	0.05	0.14
SN	–	–	–	1025.89
Total $\chi^2_{\min}$	949.48	2025.37	2025.36	3053.67
$\Delta\chi^2_{\min}$	−0.26	−3.88	−7.39	−4.51
ΛCDM$+N_{\text{eff}}$	Base	Base+LSS	Base+LSS+S$_8$	Base+LSS+S$_8$+SN
SPT-3G	519.80	519.67	519.32	522.0
Planck TT, $\ell < 30$	20.95	21.80	21.67	21.61
Planck TT, $30 \leq \ell < 1000$	403.36	403.83	404.88	407.71
Lens	5.54	5.59	5.54	5.54
τ-prior	0.01	0.26	0.56	0.91
LSS, full-shape	–	1070.78	1072.16	1074.33
LSS, BAO	–	7.28	7.52	7.50
S$_8$	–	–	1.39	1.51
SN	–	–	–	1026.99
Total $\chi^2_{\min}$	949.67	2029.22	2033.01	3068.10
$\Delta\chi^2_{\min}$	−0.07	−0.04	+0.26	−1.68

We repeat a MCMC analysis with uniform priors imposed on $\log_{10}(1 + z_{\text{tr}})$ and $\log_{10}\Delta_{\text{tr}}$, namely

$$\log_{10}(1 + z_{\text{tr}}) \in [0, 1.041],$$
$$\log_{10}\Delta_{\text{tr}} \in [-1, 1]. \tag{29}$$

Note that the bounds on $\log_{10}(1 + z_{\text{tr}})$ and the upper limit on $\log_{10}\Delta_{\text{tr}}$ are chosen to match (22). We keep the flat priors on w_0 and w_1 as in (22). To showcase the impact of the new priors, we examine the parameter constraints inferred from the Base + LSS + S$_8$ + SH0ES

Table 17. $\chi^2_{\min}$ values for the best-fit PDE and TDE models to the Base+LSS, Base+LSS+S_8, Base+LSS+S_8+SH0ES and Base + LSS + S_8 + SN datasets

PDE	Base+LSS	Base+LSS +S_8	Base+LSS +S_8+SH0ES	Base+LSS +S_8+SN
SPT-3G	519.34	519.63	519.25	519.02
Planck TT, $\ell < 30$	21.30	21.31	21.22	20.86
Planck TT, $30 \leq \ell < 1000$	403.71	403.66	403.65	404.32
Lens	6.76	6.72	6.76	6.44
τ-prior	0.24	0.01	0.00	0.07
LSS, full-shape	1056.46	1056.44	1057.70	1069.29
LSS, BAO	9.00	9.00	10.69	7.93
S_8	–	5.35	0.01	0.60
SH0ES	–	–	211.26	–
SN	–	–	–	1026.54
Total $\chi^2_{\min}$	2016.57	2016.57	2230.55	3055.07
$\Delta\chi^2_{\min}$	-12.68	-16.18	-27.39	-3.31
TDE	Base+LSS	Base+LSS +S_8	Base+LSS +S_8+SH0ES	Base+LSS +S_8+SN
SPT-3G	519.341	519.11	519.30	519.48
Planck TT, $\ell < 30$	21.37	21.12	21.08	21.25
Planck TT, $30 \leq \ell < 1000$	405.42	405.81	403.71	403.66
Lens	6.61	7.13	6.87	7.21
τ-prior	0.00	0.20	0.01	0.10
LSS, full-shape	1056.59	1057.26	1057.76	1070.55
LSS, BAO	9.24	10.54	10.46	7.40
S_8	–	0.15	0.04	0.16
SH0ES	–	–	209.71	–
SN	–	–	–	1025.76
Total $\chi^2_{\min}$	2018.57	2021.33	2228.95	3055.55
$\Delta\chi^2_{\min}$	-10.68	-11.42	-28.99	-2.83

data which demonstrate the most prominent transition in the dark energy equation of state (see Fig. 12). The parameter constraints are tabulated in Tab. 15. The corresponding 2d posterior distributions are shown in Fig. 18.

We found that uniform priors on $\log_{10}(1 + z_{\text{tr}})$ and $\log_{10} \Delta_{\text{tr}}$ impose a stronger preference for *small* values of z_{tr} and Δ_{tr}. This effect is not surprising since the logarithmic priors imply strong weight toward small z_{tr} and Δ_{tr} values. The best-fit parameter values given in Tab. 15 indicate that the TDE dynamics remains essentially unchanged. We found the difference in the best-fit χ^2 statistics between these two analyses to be not significant, namely

$$\Delta\chi^2_{\min} =$$
$$= \chi^2_{\min}(\text{New priors}) - \chi^2_{\min}(\text{Baseline priors}) = -0.5.$$

Our findings demonstrate a modest impact of the TDE priors on the dark energy parameters. The ΛCDM parameter constraints are robust against the choice of the TDE priors.

F. $\chi^2_{\min}$ PER EXPERIMENT

In this appendix we provide the best-fit $\chi^2_{\min}$ values per experiment. Table 16 presents the results for the ΛCDM, ΛCDM$+\sum m_\nu$ and ΛCDM$+N_{\text{eff}}$ models, whereas Tab. 17 shows the results in the PDE and TDE scenarios.

REFERENCES

1. E. Abdalla et al., *titleCosmology Intertwined: A Review of the Particle Physics, Astrophysics, and Cosmology Associated with the Cosmological Tensions and Anomalies*, JHEAp **34**, 49, arXiv:astro-ph.CO/2203.06142 (2022).

2. A. G. Riess, S. Casertano, W. Yuan, J. B. Bowers, L. Macri, J. C. Zinn, and D. Scolnic, *titleCosmic Distances Calibrated to 1% Precision with Gaia EDR3 Parallaxes and Hubble Space Telescope Photometry of 75 Milky Way Cepheids Confirm Tension with ΛCDM*, Astrophys. J. Lett. **908**, L6, arXiv:astro-ph.CO/2012.08534 (2021).

3. N. Aghanim et al. (collaborationPlanck), *titlePlanck 2018 Results. VI. Cosmological Parameters*, Astron. Astrophys. **641**, A6, arXiv:astro-ph.CO/1807.06209 (2020).

4. A. G. Riess et al., *titleA Comprehensive Measurement of the Local Value of the Hubble Constant with 1 km/s/Mpc Uncertainty from the Hubble Space Telescope and the SH0ES Team*, Astrophys. J. Lett. **934**, L7, arXiv:astro-ph.CO/2112.04510 (2022).

5. W. L. Freedman, B. F. Madore, T. Hoyt, I. S. Jang, R. Beaton, M. G. Lee, A. Monson, J. Neeley, and J. Rich, *titleCalibration of the Tip of the Red Giant Branch (TRGB)*, (2020), arXiv:astro-ph.GA/2002.01550.

6. K. C. Wong et al., *titleH0LiCOW – XIII. A 2.4 per Cent Measurement of H0 from Lensed Quasars: 5.3σ Tension between Early- and Late-Universe Probes*, Mon. Not. Roy. Astron. Soc. **498**, 1420, arXiv:astro-ph.CO/1907.04869 (2020).

7. S. Birrer et al., *titleTDCOSMO - IV. Hierarchical Time-Delay Cosmography – Joint Inference of the Hubble Constant and Galaxy Density Profiles*, Astron. Astrophys. **643**, A165, arXiv:astro-ph.CO/2007.02941 (2020).

8. E. Di Valentino et al., *titleCosmology Intertwined III: $f\sigma_8$ and S_8*, arXiv:astro-ph.CO/2008.11285.

9. T. M. C. Abbott et al. (collaborationDES), *titleDark Energy Survey Year 3 Results: Cosmological Constraints from Galaxy Clustering and Weak Lensing*, arXiv:astro-ph.CO/2105.13549.

10. M. Asgari et al. (collaborationKiDS), *titleKiDS-1000 Cosmology: Cosmic Shear Constraints and Comparison between Two Point Statistics*, Astron. Astrophys. **645**, A104, arXiv:astro-ph.CO/2007.15633 (2021).

11. R. Dalal et al., *titleHyper Suprime-Cam Year 3 Results: Cosmology from Cosmic Shear Power Spectra*, arXiv:astro-ph.CO/2304.00701.

12. O. H. E. Philcox and M. M. Ivanov, *titleThe BOSS DR12 Full-Shape Cosmology: ΛCDM Constraints from the Large-Scale Galaxy Power Spectrum and Bispectrum Monopole*, arXiv:astro-ph.CO/2112.04515.

13. R. C. Nunes and S. Vagnozzi, *titleArbitrating the S8 Discrepancy with Growth Rate Measurements from Redshift-Space Distortions*, Mon. Not. Roy. Astron. Soc. **505**, 5427, arXiv:astro-ph.CO/2106.01208 (2021).

14. N. Aghanim et al. (collaborationPlanck), *titlePlanck Intermediate Results. LI. Features in the Cosmic Microwave Background Temperature Power Spectrum and Shifts in Cosmological Parameters*, Astron. Astrophys. **607**, A95, arXiv:astro-ph.CO/1608.02487 (2017).

15. P. Motloch and W. Hu, *titleLensinglike Tensions in the Planck Legacy Release*, Phys. Rev. **D101**, 083515, arXiv:astro-ph.CO/1912.06601 (2020).

16. D. Dutcher et al. (collaborationSPT-3G), *titleMeasurements of the E-Mode Polarization and Temperature-E-Mode Correlation of the CMB from SPT-3G 2018 Data*, arXiv:astro-ph.CO/2101.01684.

17. S. Aiola et al. (collaborationACT), *titleThe Atacama Cosmology Telescope: DR4 Maps and Cosmological Parameters*, JCAP **12**, 047, arXiv:astro-ph.CO/2007.07288 (2020).

18. A. Chudaykin, D. Gorbunov, and N. Nedelko, *titleCombined Analysis of Planck and SPTPol Data Favors the Early Dark Energy Models*, JCAP **2008**, 013, arXiv:astro-ph.CO/2004.13046 (2020).

19. A. Chudaykin, D. Gorbunov, and N. Nedelko, *titleExploring an Early Dark Energy Solution to the Hubble Tension with Planck and SPTPol Data*, Phys. Rev. D **103**, 043529, arXiv:astro-ph.CO/2011.04682 (2021).

20. W. Yang, S. Pan, E. Di Valentino, E. N. Saridakis, and S. Chakraborty, *titleObservational Constraints on One-Parameter Dynamical Dark-Energy Parametrizations and the H_0 Tension*, Phys. Rev. D **99**, 043543, arXiv:astro-ph.CO/1810.05141 (2019).

21. E. Di Valentino, A. Melchiorri, and J. Silk, *titleCosmological Constraints in Extended Parameter Space from the Planck 2018 Legacy Release*, JCAP **01**, 013, arXiv:astro-ph.CO/1908.01391 (2020).

22. S. Vagnozzi, *titleNew physics in light of the H_0 tension: An alternative view*, Phys. Rev. D **102**, 023518, arXiv:astro-ph.CO/1907.07569 (2020).

23. R. E. Keeley, S. Joudaki, M. Kaplinghat, and D. Kirkby, *titleImplications of a Transition in the Dark Energy Equation of State for the H_0 and σ_8 Tensions*, JCAP **12**, 035, arXiv:astro-ph.CO/1905.10198 (2019).

24. W. Yang, E. Di Valentino, S. Pan, Y. Wu, and J. Lu, *titleDynamical Dark Energy after Planck CMB Final Release and H_0 Tension*, Mon. Not. Roy. Astron. Soc. **501**, 5845, arXiv:astro-ph.CO/2101.02168 (2021).

25. N. Roy, S. Goswami, and S. Das, *titleQuintessence or Phantom: Study of Scalar Field Dark Energy Models through a General Parametrization of the Hubble Parameter*, Phys. Dark Univ. **36**, 101037, arXiv:astro-ph.CO/2201.09306 (2022).

26. R. K. Sharma, K. L. Pandey, and S. Das, *titleImplications of an Extended Dark Energy Model with Massive Neutrinos*, Astrophys. J. **934**, 113, arXiv:astro-ph.CO/2202.01749 (2022).

27. G.-B. Zhao, R. G. Crittenden, L. Pogosian, and X. Zhang, *titleExamining the Evidence for Dynamical Dark Energy*, Phys. Rev. Lett. **109**, 171301, arXiv:astro-ph.CO/1207.3804 (2012).

28. G.-B. Zhao et al., *titleDynamical Dark Energy in Light of the Latest Observations*, Nature Astron. **1**, 627, arXiv:astro-ph.CO/1701.08165 (2017).

29. Y. Wang, L. Pogosian, G.-B. Zhao, and A. Zucca, *titleEvolution of Dark Energy Reconstructed from the Latest Observations*, Astrophys. J. Lett. **869**, L8, arXiv:astro-ph.CO/1807.03772 (2018).

30. K. Dutta, Ruchika, A. Roy, A. A. Sen, and M. M. Sheikh-Jabbari, *titleBeyond ΛCDM with Low and High Redshift Data: Implications for Dark Energy*, Gen. Rel. Grav. **52**, 15, arXiv:astro-ph.CO/1808.06623 (2020).

31. S. Capozziello, Ruchika, and A. A. Sen, *titleModel Independent Constraints on Dark Energy Evolution from Low-Redshift Observations*, Mon. Not. Roy. Astron. Soc. **484**, 4484, arXiv:astro-ph.CO/1806.03943 (2019).

32. L. Heisenberg, H. Villarrubia-Rojo, and J. Zosso, *titleSimultaneously Solving the H_0 and σ_8 Tensions with Late Dark Energy*, arXiv:astro-ph.CO/2201.11623.

33. G. Alestas and L. Perivolaropoulos, *titleLate-Time Approaches to the Hubble Tension Deforming H(z), Worsen the Growth Tension*, Mon. Not. Roy. Astron. Soc. **504**, 3956, arXiv:astro-ph.CO/2103.04045 (2021).

34. E. Di Valentino, A. Mukherjee, and A. A. Sen, *titleDark Energy with Phantom Crossing and the H_0 Tension*, Entropy **23**, 404, arXiv:astro-ph.CO/2005.12587 (2021).

35. H. K. Jassal, J. S. Bagla, and T. Padmanabhan, *titleUnderstanding the Origin of CMB Constraints on Dark Energy*, Mon. Not. Roy. Astron. Soc. **405**, 2639, /astro-ph/0601389 (2010).

36. J. Henning et al. (collaborationSPT), *titleMeasurements of the Temperature and E-Mode Polarization of the CMB from 500 Square Degrees of SPTpol Data*, Astrophys. J. **852**, 97, arXiv:astro-ph.CO/1707.09353 (2018).

37. M. M. Ivanov, M. Simonović, and M. Zaldarriaga, *titleCosmological Parameters from the BOSS Galaxy Power Spectrum*, arXiv:astro-ph.CO/1909.05277.

38. M. M. Ivanov, O. H. E. Philcox, M. Simonović, M. Zaldarriaga, T. Nishimichi, and M. Takada, *titleCosmological Constraints without Fingers of God*, arXiv:astro-ph.CO/2110.00006.

39. O. H. E. Philcox, M. M. Ivanov, M. Simonović, and M. Zaldarriaga, *titleCombining Full-Shape and BAO Analyses of Galaxy Power Spectra: A 1.6\% CMB-independent Constraint on H_0*, JCAP **05**, 032, arXiv:astro-ph.CO/2002.04035 (2020).

40. A. Chudaykin, M. M. Ivanov, O. H. E. Philcox, and M. Simonovi?, *titleNon-linear Perturbation Theory Extension of the Boltzmann Code CLASS*, Phys. Rev. **D102**, 063533, arXiv:astro-ph.CO/2004.10607 (2020).

41. B. Audren, J. Lesgourgues, K. Benabed, and S. Prunet, *titleConservative Constraints on Early Cosmology: An Illustration of the Monte Python Cosmological Parameter Inference Code*, JCAP **1302**, 001, arXiv:astro-ph.CO/1210.7183 (2013).

42. T. Brinckmann and J. Lesgourgues, *titleMontePython 3: Boosted MCMC Sampler and Other Features*, Phys. Dark Univ. **24**, 100260, arXiv:astro-ph.CO/1804.07261 (2019).

43. A. Lewis and S. Bridle, *titleCosmological Parameters from CMB and Other Data: A Monte Carlo Approach*, Phys. Rev. D **66**, 103511, /astro-ph/0205436 (2002).

44. A. Lewis, *titleEfficient Sampling of Fast and Slow Cosmological Parameters*, Phys. Rev. D **87**, 103529, arXiv:astro-ph.CO/1304.4473 (2013).

45. A. Lewis, *titleGetDist: A Python Package for Analysing Monte Carlo Samples*, arXiv:astro-ph.IM/1910.13970.

46. W. L. K. Wu et al., *titleA Measurement of the Cosmic Microwave Background Lensing Potential and Power Spectrum from 500 deg^2 of SPTpol Temperature and Polarization Data*, Astrophys. J. **884**, 70, arXiv:astro-ph.CO/1905.05777 (2019).

47. R. De Belsunce, S. Gratton, W. Coulton, and G. Efstathiou, *titleInference of the Optical Depth to Reionization from Low Multipole Temperature and Polarisation Planck Data*, arXiv:astro-ph.CO/2103.14378.

48. O. H. E. Philcox, *titleCosmology without Window Functions: Quadratic Estimators for the Galaxy Power Spectrum*, Phys. Rev. D **103**, 103504, arXiv:astro-ph.CO/2012.09389 (2021).

49. O. H. E. Philcox, *titleCosmology without Window Functions. II. Cubic Estimators for the Galaxy Bispectrum*, Phys. Rev. D **104**, 123529, arXiv:astro-ph.CO/2107.06287 (2021).

50. F. Beutler and P. McDonald, *titleUnified Galaxy Power Spectrum Measurements from 6dFGS, BOSS, and eBOSS*, JCAP **11**, 031, arXiv:astro-ph.CO/2106.06324 (2021).

51. A. Chudaykin, K. Dolgikh, and M. M. Ivanov, *titleConstraints on the Curvature of the Universe and Dynamical Dark Energy from the Full-Shape and BAO Data*, Phys. Rev. D **103**, 023507, arXiv:astro-ph.CO/2009.10106 (2021).

52. T. Nishimichi, G. D'Amico, M. M. Ivanov, L. Senatore, M. Simonović, M. Takada, M. Zaldarriaga, and P. Zhang, *titleBlinded Challenge for Precision Cosmology with Large-Scale Structure: Results from Effective Field Theory for the Redshift-Space Galaxy Power Spectrum*, Phys. Rev. D **102**, 123541, arXiv:astro-ph.CO/2003.08277 (2020).

53. G. D'Amico, J. Gleyzes, N. Kokron, K. Markovic, L. Senatore, P. Zhang, F. Beutler, and H. Gil-Marín, *titleThe Cosmological Analysis of the SDSS/BOSS data from the Effective Field Theory of Large-Scale Structure*, JCAP **05**, 005, arXiv:astro-ph.CO/1909.05271 (2020).

54. M. M. Ivanov, O. H. E. Philcox, T. Nishimichi, M. Simonović, M. Takada, and M. Zaldarriaga, *titlePrecision Analysis of the Redshift-Space Galaxy Bispectrum*, Phys. Rev. D **105**, 063512, arXiv:astro-ph.CO/2110.10161 (2022).

55. A. J. Ross, L. Samushia, C. Howlett, W. J. Percival, A. Burden, and M. Manera, *titleThe Clustering of the SDSS DR7 Main Galaxy Sample – I. a 4 per Cent Distance Measure at $z = 0.15$*, Mon. Not. Roy. Astron. Soc. **449**, 835, arXiv:astro-ph.CO/1409.3242 (2015).

56. F. Beutler, C. Blake, M. Colless, D. H. Jones, L. Staveley-Smith, L. Campbell, Q. Parker, W. Saunders, and F. Watson, *titleThe 6dF Galaxy Survey: Baryon Acoustic Oscillations and the Local Hubble Constant*, Mon. Not. Roy. Astron. Soc. **416**, 3017, arXiv:astro-ph.CO/1106.3366 (2011).

57. R. Neveux et al., *titleThe Completed SDSS-IV Extended Baryon Oscillation Spectroscopic Survey: BAO and RSD Measurements from the Anisotropic Power Spectrum of the Quasar Sample between Redshift 0.8 and 2.2*, Mon. Not. Roy. Astron. Soc. **499**, 210, arXiv:astro-ph.CO/2007.08999 (2020).

58. H. du Mas des Bourboux et al., *titleThe Completed SDSS-IV Extended Baryon Oscillation Spectroscopic Survey: Baryon Acoustic Oscillations with Lyα Forests*, Astrophys. J. **901**, 153, arXiv:astro-ph.CO/2007.08995 (2020).

59. A. de Mattia et al., *titleThe Completed SDSS-IV Extended Baryon Oscillation Spectroscopic Survey: Measurement of the BAO and Growth Rate of Structure of the Emission Line Galaxy Sample from the Anisotropic Power Spectrum between Redshift 0.6 and 1.1*, Mon. Not. Roy. Astron. Soc. **501**, 5616, arXiv:astro-ph.CO/2007.09008 (2021).

60. M. M. Ivanov, *titleCosmological Constraints from the Power Spectrum of eBOSS Emission Line Galaxies*, Phys. Rev. D **104**, 103514, arXiv:astro-ph.CO/2106.12580 (2021).

61. C. Hikage et al. (collaborationHSC), *titleCosmology from Cosmic Shear Power Spectra with Subaru Hyper Suprime-Cam First-Year Data*, Publ. Astron. Soc. Jap. **71**, 43, arXiv:astro-ph.CO/1809.09148 (2019).

62. K. L. Greene and F.-Y. Cyr-Racine, *titleHubble Distancing: Focusing on Distance Measurements in Cosmology*, JCAP **06**, 002, arXiv:astro-ph.CO/2112.11567 (2022).

63. D. Camarena and V. Marra, *titleOn the Use of the Local Prior on the Absolute Magnitude of Type Ia Supernovae in Cosmological Inference*, Mon. Not. Roy. Astron. Soc. **504**, 5164, arXiv:astro-ph.CO/2101.08641 (2021).

64. D. M. Scolnic et al. (collaborationPan-STARRS1), *titleThe Complete Light-curve Sample of Spectroscopically Confirmed SNe Ia from Pan-STARRS1 and Cosmological Constraints from the Combined Pantheon Sample*, Astrophys. J. **859**, 101, arXiv:astro-ph.CO/1710.00845 (2018).

65. P. Lemos, E. Lee, G. Efstathiou, and S. Gratton, *titleModel Independent $H(z)$ Reconstruction Using the Cosmic Inverse Distance Ladder*, Mon. Not. Roy. Astron. Soc. **483**, 4803, arXiv:astro-ph.CO/1806.06781 (2019).

66. V. Poulin, K. K. Boddy, S. Bird, and M. Kamionkowski, *titleImplications of an Extended Dark Energy Cosmology with Massive Neutrinos for Cosmological Tensions*, Phys. Rev. D **97**, 123504, arXiv:astro-ph.CO/1803.02474 (2018).

67. B. R. Dinda, *titleCosmic Expansion Parametrization: Implication for Curvature and H0 Tension*, Phys. Rev. D **105**, 063524, arXiv:astro-ph.CO/2106.02963 (2022).

68. R. E. Keeley and A. Shafieloo, *titleRuling Out New Physics at Low Redshift as a Solution to the H_0 Tension*, arXiv:astro-ph.CO/2206.08440.

69. M. M. Schmittfull, A. Challinor, D. Hanson, and A. Lewis, *titleJoint analysis of CMB temperature and lensing-reconstruction power spectra*, Phys. Rev. D **88**, 063012, arXiv:astro-ph.CO/1308.0286 (2013).

70. J. Peloton, M. Schmittfull, A. Lewis, J. Carron, and O. Zahn, *titleFull Covariance of CMB and Lensing Reconstruction Power Spectra*, Phys. Rev. D **95**, 043508, arXiv:astro-ph.CO/1611.01446 (2017).

71. G. Addison, Y. Huang, D. Watts, C. Bennett, M. Halpern, G. Hinshaw, and J. Weiland, *titleQuantifying Discordance in the 2015 Planck CMB Spectrum*, Astrophys. J. **818**, 132, arXiv:astro-ph.CO/1511.00055 (2016).

72. N. Aghanim et al. (collaborationPlanck), *titlePlanck 2015 Results. XI. CMB Power Spectra, Likelihoods, and Robustness of Parameters*, Astron. Astrophys. **594**, A11, arXiv:astro-ph.CO/1507.02704 (2016).

73. F. Bianchini et al. (collaborationSPT), *titleConstraints on Cosmological Parameters from the 500 deg^2 SPTpol Lensing Power Spectrum*, Astrophys. J. **888**, 119, arXiv:astro-ph.CO/1910.07157 (2020).

74. P. Motloch and W. Hu, *titleTensions between Direct Measurements of the Lens Power Spectrum from Planck Data*, Phys. Rev. D **97**, 103536, arXiv:astro-ph.CO/1803.11526 (2018).

75. E. Di Valentino and A. Melchiorri, *titleNeutrino Mass Bounds in the Era of Tension Cosmology*, arXiv:astro-ph.CO/2112.02993.

76. H. Akaike, *titleA new look at the statistical model identification*, IEEE Transactions on Automatic Control **19**, 716 (1974), doi:10.1109/TAC.1974.1100705.

77. T. Delubac et al. (collaborationBOSS), *titleBaryon Acoustic Oscillations in the Lyα Forest of BOSS DR11 Quasars*, Astron. Astrophys. **574**, A59, arXiv:astro-ph.CO/1404.1801 (2015).

78. R. C. Bernardo, D. Grandón, J. L. Said, and V. H. Cárdenas, *titleParametric and Nonparametric Methods Hint Dark Energy Evolution*, arXiv:astro-ph.CO/2111.08289.

79. G. Efstathiou, *titleTo H0 or Not to H0?*, Mon. Not. Roy. Astron. Soc. **505**, 3866, arXiv:astro-ph.CO/2103.08723 (2021).

80. G. Benevento, W. Hu, and M. Raveri, *titleCan Late Dark Energy Transitions Raise the Hubble Constant?*, Phys. Rev. D **101**, 103517, arXiv:astro-ph.CO/2002.11707 (2020).

81. E. Macaulay et al. (collaborationDES), *titleFirst Cosmological Results using Type Ia Supernovae from the Dark Energy Survey: Measurement of the Hubble Constant*, Mon. Not. Roy. Astron. Soc. **486**, 2184, arXiv:astro-ph.CO/1811.02376 (2019).

82. S. M. Feeney, H. V. Peiris, A. R. Williamson, S. M. Nissanke, D. J. Mortlock, J. Alsing, and D. Scolnic, *titleProspects for Resolving the Hubble Constant Tension with Standard Sirens*, Phys. Rev. Lett. **122**, 061105, arXiv:astro-ph.CO/1802.03404 (2019).

83. D. Camarena and V. Marra, *titleA New Method to Build the (Inverse) Distance Ladder*, Mon. Not. Roy. Astron. Soc. **495**, 2630, arXiv:astro-ph.CO/1910.14125 (2020).

84. M. Rigault et al. (collaborationNearby Supernova factory), *titleEvidence of Environmental Dependencies of Type Ia Supernovae from the Nearby Supernova Factory indicated by Local Hα*, Astron. Astrophys. **560**, A66, arXiv:astro-ph.CO/1309.1182 (2013).

85. M. Rigault et al., *titleConfirmation of a Star Formation Bias in Type Ia Supernova Distances and its Effect on Measurement of the Hubble Constant*, Astrophys. J. **802**, 20, arXiv:astro-ph.CO/1412.6501 (2015).

86. M. Rigault et al. (collaborationNearby Supernova Factory), *titleStrong Dependence of Type Ia Supernova Standardization on the Local Specific Star Formation Rate*, Astron. Astrophys. **644**, A176, arXiv:astro-ph.CO/1806.03849 (2020).

87. M. Briday et al., *titleAccuracy of Environmental Tracers and Consequences for Determining the Type Ia Supernova Magnitude Step*, Astron. Astrophys. **657**, A22, arXiv:astro-ph.CO/2109.02456 (2022).

88. D. O. Jones, A. G. Riess, and D. M. Scolnic, *titleReconsidering the Effects of Local Star Formation On Type Ia Supernova Cosmology*, Astrophys. J. **812**, 31, arXiv:astro-ph.CO/1506.02637 (2015).

89. D. O. Jones et al. (collaborationFSS), *titleThe Foundation Supernova Survey: Measuring Cosmological Parameters with Supernovae from a Single Telescope*, Astrophys. J. **881**, 19, arXiv:astro-ph.CO/1811.09286 (2019).

90. A. G. Riess et al., *titleA 2.4% Determination of the Local Value of the Hubble Constant*, Astrophys. J. **826**, 56, arXiv:astro-ph.CO/1604.01424 (2016).

91. A. G. Riess, S. Casertano, W. Yuan, L. M. Macri, and D. Scolnic, *titleLarge Magellanic Cloud Cepheid Standards Provide a 1% Foundation for the Determination of the Hubble Constant and Stronger Evidence for Physics beyond ΛCDM*, Astrophys. J. **876**, 85, arXiv:astro-ph.CO/1903.07603 (2019).

92. L. Perivolaropoulos and F. Skara, *titleHubble Tension or a Transition of the Cepheid SnIa Calibrator Parameters?*, Phys. Rev. D **104**, 123511, arXiv:astro-ph.CO/2109.04406 (2021).

93. E. Mortsell, A. Goobar, J. Johansson, and S. Dhawan, *titleSensitivity of the Hubble Constant Determination to Cepheid Calibration*, Astrophys. J. **933**, 212, arXiv:astro-ph.CO/2105.11461 (2022).

94. E. Mortsell, A. Goobar, J. Johansson, and S. Dhawan, *titleThe Hubble Tension Revisited: Additional Local Distance Ladder Uncertainties*, Astrophys. J. **935**, 58, arXiv:astro-ph.CO/2106.09400 (2022).

95. V. Marra and L. Perivolaropoulos, *titleRapid Transition of Geff at $zt \simeq 0.01$ as a Possible Solution of the Hubble and Growth Tensions*, Phys. Rev. D **104**, L021303, arXiv:astro-ph.CO/2102.06012 (2021).

96. G. Alestas, L. Kazantzidis, and L. Perivolaropoulos, *titlew − M Phantom Transition at $z_t <0.1$ as a Resolution of the Hubble Tension*, Phys. Rev. D **103**, 083517, arXiv:astro-ph.CO/2012.13932 (2021).

97. J. L. Bernal, L. Verde, and A. G. Riess, *titleThe Trouble with H_0*, JCAP **10**, 019, arXiv:astro-ph.CO/1607.05617 (2016).

98. Y.-P. Teng, W. Lee, and K.-W. Ng, *titleConstraining the Dark-Energy Equation of State with Cosmological Data*, Phys. Rev. D **104**, 083519, arXiv:astro-ph.CO/2105.02667 (2021).

99. R. Trotta, *titleBayes in the sky: Bayesian inference and model selection in cosmology*, Contemp. Phys. **49**, 71, arXiv:astro-ph/0803.4089 (2008).

100. A. Heavens, Y. Fantaye, A. Mootoovaloo, H. Eggers, Z. Hosenie, S. Kroon, and E. Sellentin, *titleMarginal Likelihoods from Monte Carlo Markov Chains*, arXiv:stat.CO/1704.03472.

101. R. E. Kass and A. E. Raftery, *titleBayes Factors*, J. Am. Statist. Assoc. **90**, 773 (1995), doi:10.1080/01621459.1995.10476572.

102. P. Ade et al. (collaborationSimons Observatory), *titleThe Simons Observatory: Science Goals and Forecasts*, JCAP **02**, 056, arXiv:astro-ph.CO/1808.07445 (2019).

103. K. N. Abazajian et al. (collaborationCMB-S4), *titleCMB-S4 Science Book, First Edition*, arXiv:astro-ph.CO/1610.02743.

104. L. Balkenhol et al. (collaborationSPT-3G), *titleA Measurement of the CMB Temperature Power Spectrum and Constraints on Cosmology from the SPT-3G 2018 TT/TE/EE Data Set*, arXiv:astro-ph.CO/2212.05642.

105. T. Simon, P. Zhang, and V. Poulin, *titleCosmological Inference from the EFTofLSS: the eBOSS QSO Full-Shape Analysis*, arXiv:astro-ph.CO/2210.14931.

106. A. Chudaykin and M. M. Ivanov, *titleCosmological Constraints from the Power Spectrum of eBOSS Quasars*, Phys. Rev. D **107**, 043518, arXiv:astro-ph.CO/2210.17044 (2023).

107. M. M. Ivanov, O. H. E. Philcox, G. Cabass, T. Nishimichi, M. Simonović, and M. Zaldarriaga, *titleCosmology with the Galaxy Bispectrum Multipoles: Optimal Estimation and Application to BOSS Data*, arXiv:astro-ph.CO/2302.04414.